Single-cell dynamics reveal a stress-induced decision between cardiomyocyte hypertrophy and apoptosis

Bryan Chun[1], Lavie Ngo[1], Jeffrey J. Saucerman[1]*

[1]Department of Biomedical Engineering and Robert M. Berne Cardiovascular Research Center, University of Virginia, Charlottesville, VA 22908, USA

*Corresponding author: jsaucerman@virginia.edu

Summary

Cardiomyocyte hypertrophy and apoptosis underlie cardiomyopathies and heart failure. While previous studies have described hypertrophy or apoptosis at the level of cell populations, how individual cells commit to these distinct yet co-regulated fates is unclear. We developed a high-content microscopy approach to track single-cell hypertrophy and apoptosis dynamics, revealing new features and unique subpopulation responses. The catecholamine isoproterenol induced both analog hypertrophy and digital apoptosis. While high-dose isoproterenol induced mixed hypertrophy and apoptosis at the population level, we found that individual cells that hypertrophy are more likely to survive. Likewise, phenylephrine-induced hypertrophy was associated with survival at the single-cell level. Inhibiting caspase-3 reduced apoptosis and increased a cell's likelihood of hypertrophy. Multinomial log-linear models demonstrate that a cell's initial size and DNA content predict its susceptibility to hypertrophy or apoptosis. These data support a "grow or die" conceptual model for cardiomyocyte decisions. This work develops a single-cell profiling method to reveal that while hypertrophy and apoptosis often coincide at the population level, single cells that hypertrophy are protected from death.

Introduction

Cells utilize a finite number of signaling pathways and intermediates to determine a multitude of cell fates such as developmental specification [1], [2] or drug responses [3], [4], [5]. For example, heart failure involves both cardiomyocyte hypertrophy and apoptosis [6], [7], [8]. While apoptosis has been clearly implicated in heart failure progression [9], hypertrophy can be physiological or pathological [10], [11]. Furthermore, apoptosis and hypertrophy may have interacting roles that result in the transition from physiological to pathological hypertrophy. Understanding the differential co-regulation of hypertrophy and apoptosis is critical to differentiate between pathological hypertrophy, which is accompanied by apoptosis, and compensatory hypertrophy in the absence of apoptosis [12], [13], [14], [15]. These interactions need to be better understood to develop targeted therapeutic strategies for heart failure [16].

A number of studies have shown that cardiomyocyte hypertrophy and apoptosis are co-regulated *in vivo*. For example, pressure-overload and catecholamine overstimulation induce both hypertrophy and apoptosis [17], [18], [19]. Calcineurin overexpression elicits hypertrophy that is protective against apoptosis [20], even though calcineurin directly dephosphorylates the pro-apoptotic Bcl-2 family protein BAD [21], [22]. Despite insight into population-level responses, *in vivo* studies have not elucidated the dynamic, functional relationships between hypertrophy and apoptosis at the level of single cells.

One recent technology for capturing single-cell heterogeneity is single-cell RNA sequencing, which has provided a number of important insights into health and disease [3], [4], [23]. For example, Chaffin et al. identified three distinct populations of cardiomyocytes that are differentially distributed in human hearts with dilated and hypertrophic cardiomyopathies [24].

Other studies have used single-cell RNA sequencing (scRNA-seq) to characterize cell subpopulations that regulate development, differentiation, and in response to drugs that could not be resolved with bulk measurements at the population level. Still, for most pathological responses in the heart, the dynamic and causal relationships between these co-occuring subpopulations as they respond to perturbations remains unclear [12], [25].

In this work, we propose two simple conceptual models for joint cardiomyocyte decision-making of hypertrophy and apoptosis. A “grow-and-die” model represents serial decision-making, where cells hypertrophy but then later apoptose due to an inability to handle growth stresses [26]. In contrast, the importance of caspase-mediated apoptosis but also reported sub-apoptotic caspase activity in hypertrophy [27] is consistent with a distinct parallel decision-making “grow-or-die” model based on a threshold of caspase activity [27], [28]. However, both *in vivo* and *in vitro* [29], [30], [31], [32], [33], [34] experiments have examined fixed timepoints at the population level, which does not provide the single-cell tracking that is required to discriminate between “grow-or-die” vs. “grow-and-die” conceptual models. To overcome these limitations, here, we designed a live-cell high-content microscopy approach with machine learning image analysis to track the dynamics of individual neonatal rat cardiomyocyte growth and death simultaneously. Using this high-content microscopy platform, we characterize the single-cell dynamic hypertrophy and apoptosis responses of cardiomyocytes to multiple perturbations that support the “grow-or-die” model of decision making, together with a machine learning model that identifies cell size, shape, and nuclear features that predict single-cell commitment to hypertrophy or apoptosis. Our work thus develops an experimental-machine learning framework to reveal how cells interpret stress signals based on their initial state to guide single-cell decisions of growth or death.

Results

Assay design for single-cell phenotyping of hypertrophy-apoptosis dynamics

We developed a live single-cell microscopy assay to track multiple simultaneous fluorescent readouts of hypertrophic and apoptotic activity (**Figure 1A**). Neonatal rat cardiomyocytes were transduced with an eGFP-expressing lentivirus as a live-cell reporter of single-cell morphology and protein synthesis. Nuclei were labeled with Hoechst, and general cell death and apoptosis were measured with propidium iodide (PI) and fluorescently-conjugated annexin V (A5). To measure live-cell dynamics, individual wells in a 96-well microplate representing different treatment conditions were imaged for 48 hours with a 1 hour resolution (**Figure 1B**). After live-cell imaging, cells were fixed, permeabilized, and immunostained to detect cardiomyocyte-specific □-actinin expression.

We developed machine learning image analyses to measure dynamics of multiple metrics related to cellular morphology, viability, and final □-actinin expression at a single-cell level (**Methods**). To correct for cell-to-cell eGFP expression variability and uneven fluorescence that persisted after flatfield illumination, we trained a random forest classifier to generate probability maps of eGFP (**Figure 1C**). The random forest model was robust to at least a 5-fold range in variations in fluorescence signal-to-noise ratio, allowing optimization of fluorescence acquisition settings to minimize phototoxicity (**Supplemental Figure 1**). We used this eGFP probability map for thresholding, single-cell segmentation, and tracking for longitudinal morphology and fluorescence measurements (**Figure 1D** and **Methods**). As our eGFP reporter uses a ubiquitous CMV promoter that does not differentiate between cardiomyocytes and other cell types, we tracked cardiomyocytes by first live-cell tracking in eGFP and then colocalizing eGFP with the α-actinin probability map in the fixed images. Similarly, a live A5 probability map was used to determine A5 positivity of each cell.

93 Our assay was first validated with cells treated with a DMSO negative vehicle control. Even in
94 the absence of hypertrophic or apoptotic stimuli, there was considerable single-cell variability of
95 both hypertrophic (**Figure 1A** and **D**, orange outline and traces) and apoptotic trajectories
96 (cyan outline and traces). Live single-cell tracking across 48 hours is shown in **Supplemental**
97 **Movie 1**. At the cell-population level, A5 binding accumulated earlier than PI uptake, indicating
98 that most of the death observed was due to apoptosis rather than other death processes (**Figure**
99 **1F**). This apoptotic lag between initial A5 binding and later PI uptake at the population level was
100 validated in individual A5/PI double-positive cells (**Figure 1G**).

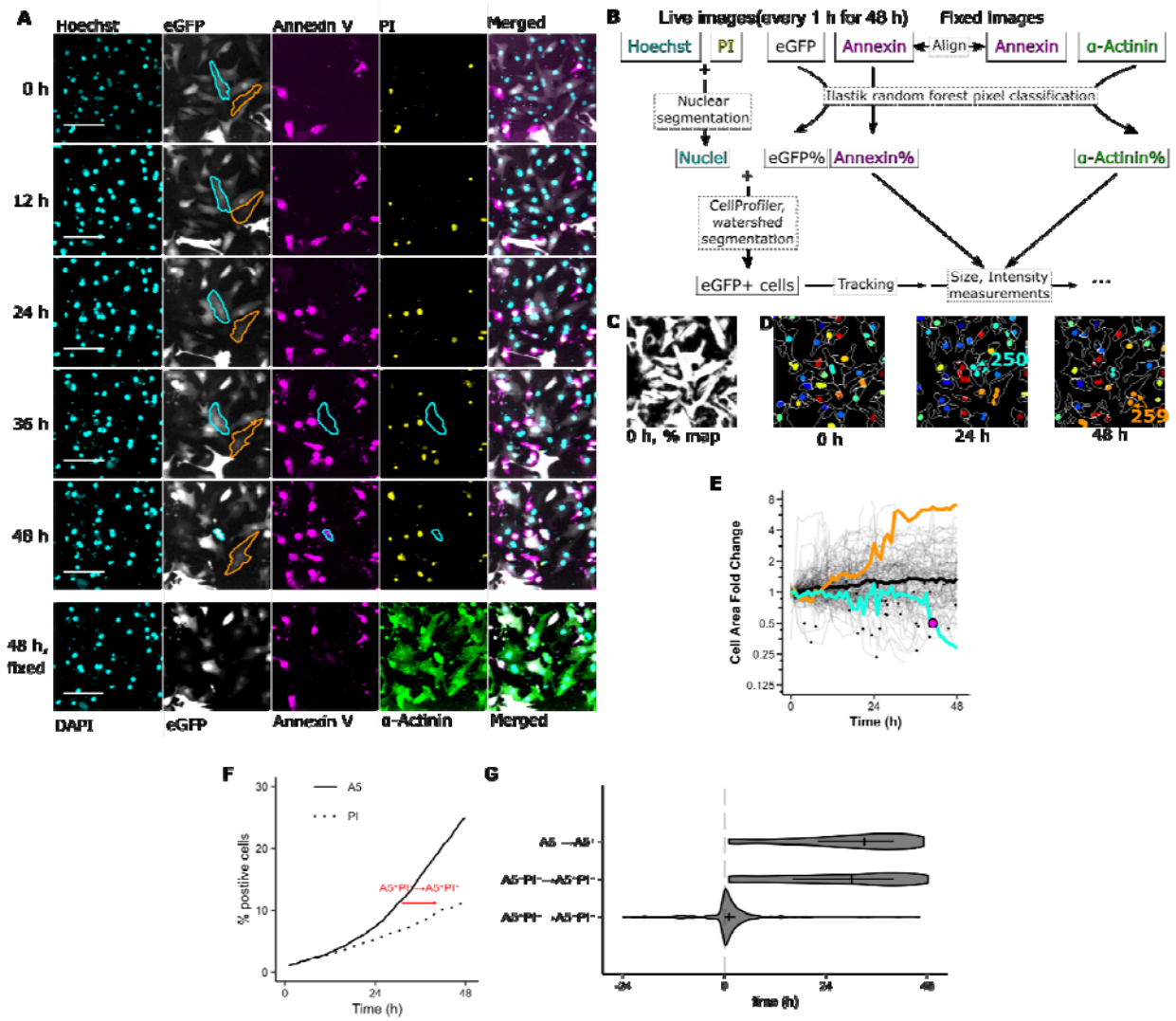

Figure 1. High-content time-lapse microscopy of single-cell morphological and apoptosis dynamics of neonatal rat cardiac myocytes.

(**A**) Representative timelapse images of neonatal rat cardiomyocytes treated with 0.1% DMSO (neg. control). Live imaging tracked changes in morphology of eGFP-expressing cells and apoptotic A5 and PI binding over 48 hours (rows 1 through 5). After two days (row 6), cells were fixed and stained for DNA (DAPI, cyan) and α-actinin (green). Outlines represent manual segmentation of cells undergoing hypertrophy (orange) or early apoptotic A5 binding and PI exclusion (cyan). Scale bar is 100 µm.

(**B**) Schematic of image analysis pipeline for single-cell cardiomyocyte hypertrophy and apoptosis dynamics.

(**C**) Example eGFP fluorescence probability map for the GFP image in (A) for image thresholding and segmentation.

(**D**) Example segmentation and tracking of cells in (A). White outlines represent automated segmentation results of eGFP cels and pseudocoloured ovals represent nuclear segmentation. The tracking of the two outlined cells in (A) are marked with their identifier (cyan and orange numbers and arrows).

(**E**) Single-cell heterogeneity in cardiomyocyte hypertrophy dynamics (black lines). Orange and cyan traces correspond to previously identified cells. Solid black line corresponds to the population median. Black dots indicate onset of A5 binding as does the large magenta dot for the cyan trace. Cell Area Fold Change reported as cell areas normalized to the average of areas measured at initial two timepoints.
(**F**) Empirical cumulative distribution function of A5 (solid line) and PI (dashed line) binding for all DMSO-treated cells (n = 3601 cells from 3 wells from each of 2 independent isolations). The rightward shift of the PI binding curve indicates later onset of PI binding in the cell population consistent with apoptosis.
(**G**). Single-cell quantification of onset of A5 and PI binding show that PI occurs after A5 binding, with the lag between those two events quantified (red distribution; * $p < .0001$, one-sample Wilcoxon signed rank test, n = 451 cells).

Cellular and nuclear profiling of staurosporine-induced apoptosis dynamics

Apoptosis is characterized by morphological and biochemical changes to both cell and nucleus. As a representative cellular perturbation to examine apoptosis dynamics with our high-content imaging assay, we used the broad spectrum ATP-competitive kinase inhibitor staurosporine (STS), which is well-known to induce apoptosis in cardiomyocytes and other cell types [35], [36], [37], [38]. STS-induced apoptotic or death markers such as A5 or PI have been characterized in fixed cardiomyocytes at a coarse time resolution [38], [39]. Our high-content imaging assay uniquely allows for simultaneous characterization and high-resolution dynamic single-cell tracking of multiple features related to apoptosis including A5 binding, PI uptake, changes in nuclei morphology, and chromatin condensation and degradation.

Treatment with STS induced substantial A5 binding and PI uptake compared to DMSO vehicle-control treatment (**Figure 2A** and **B**). Consistent with prior studies, bulk-population dynamics of total accumulation of A5 and PI were again indicative of apoptosis, with PI-uptake occurring later than that of A5 (**Figure 2C**). However, single-cell dynamics of apoptosis were markedly different between STS and DMSO treatments. DMSO treatment induced a biphasic response with initially low levels of A5 and PI binding between 0 and 24 hours and a second phase of increased apoptotic activity after 24 hours. In contrast, STS-treated cells largely completed apoptosis within the first 36 hours of treatment, as shown in **Supplemental Movie 2.** Single-

149 cell tracking revealed a positive time lag from A5 to PI binding to become A5/PI-double positive
150 (**Figure 2D**), consistent with apoptosis and not other forms of cell death. This indicates the
151 added value of measuring single-cell dynamics of cell death.

152 Next, we sought to characterize the temporal dynamics of additional cellular features that may
153 be associated with apoptosis (**Figure 2E**). As expected, STS treatment induced global increases
154 of cell membrane A5 binding followed by nuclear PI uptake. Motivated by known apoptotic
155 nuclear and chromatin changes [40], we also investigated dynamic changes in nuclear Hoechst
156 staining. Mean and total (integrated) Hoechst intensity (reflecting membrane permeability), and
157 median absolute deviation (MAD) of the Hoechst intensity (reflecting chromatin condensation)
158 all exhibited coordinated increases with STS-treatment [40], [41]. After approximately 24 hours,
159 STS-treated trajectories of Hoechst decreased below that of DMSO-treated trajectories,
160 consistent with DNA degradative apoptotic processes. We also investigated changes in nuclear
161 morphology. During the first 36 hours, nuclei of STS-treated cells had smaller nuclei, which
162 later increased in size relative to their DMSO-treated counterparts. Interestingly, nuclear form
163 factor decreased and eccentricity increased in STS-treated cells relative to DMSO-treated cells
164 even at the very early times, indicating more irregular and less circular nuclei consistent with
165 apoptosis. Overall, single-cell tracking of multiple cellular features delineates a temporal
166 sequence of apoptotic kinetics, starting with changes to nuclear permeability and shape,
167 followed by A5 binding, and finally loss of cell membrane integrity.

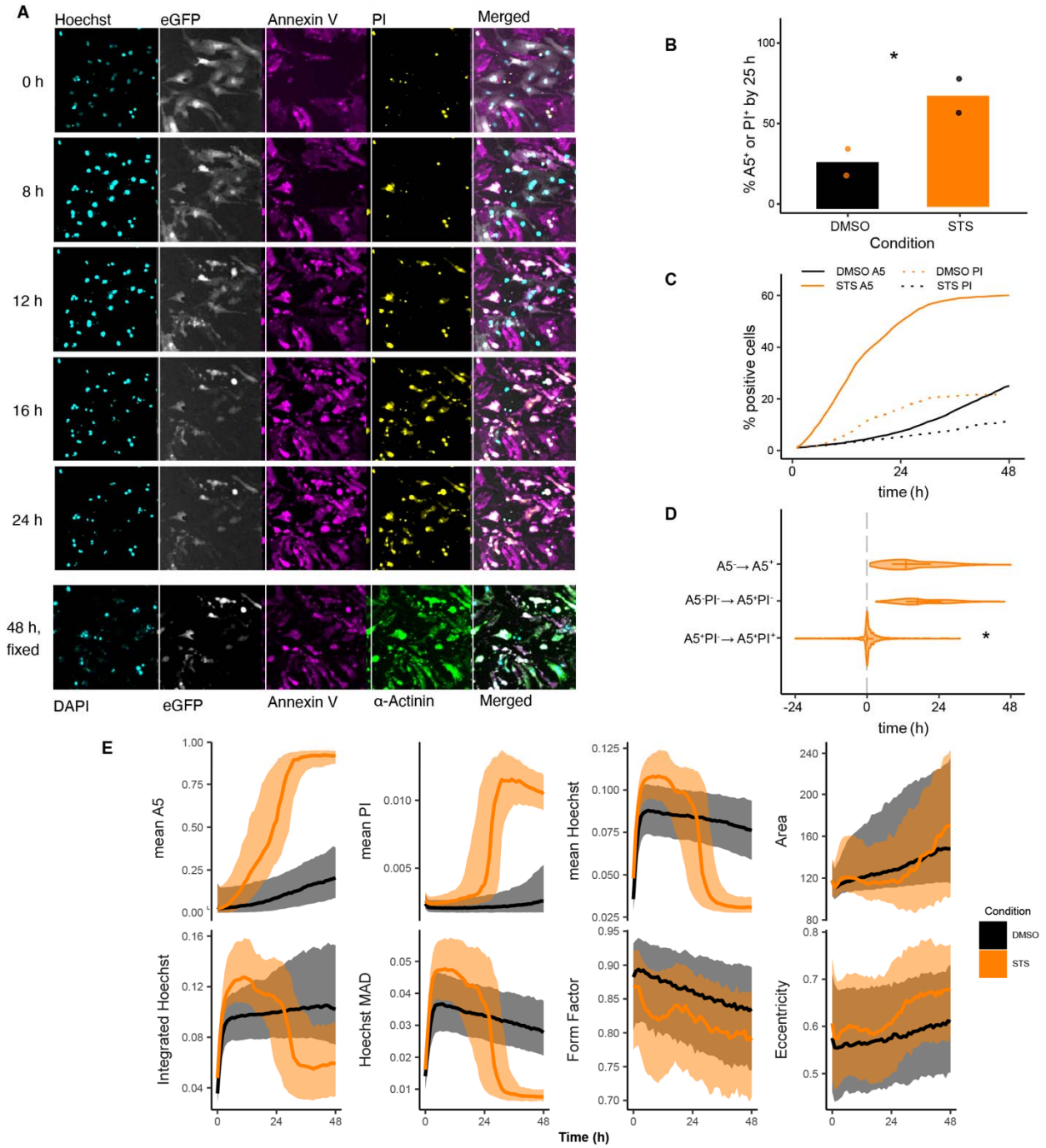

Figure 2. Single-cell dynamics show that cardiomyocyte death induced by staurosporine follows a sequence of nuclear permeability and shape, chromatin condensation, annexin 5 binding, and membrane permeability.
(**A**) Representative timelapse images of neonatal rat cardiomyocytes treated with 1 µM STS show induction of A5 and PI binding (magenta and yellow, respectively) and pyknosis (cyan).

174 (**B**) 1 µM STS increased the fraction of either A5-or PI-positive cardiomyocytes compared to the
175 0.1% DMSO vehicle control condition (* $p = 0.018$, paired Welch's one-tailed *t*-test, 2-3 wells
176 per condition for each of $n = 2$ independent cell isolations (represented as jitter points).
177 (**C**) Empirical cumulative distribution function of A5 (solid) and PI (dashed) binding for all STS-
178 treated cells. Same DMSO traces as in **Figure 1F**.
179 (**D**) Single-cell quantification of time lag from A5 binding to PI binding in response to STS
180 treatment (* $p < 10^{-11}$, one-sample Wilcoxon signed rank test, $n = 1146$ cells).
181 (**E**) Single-cell dynamics of nuclear metrics in response to either 1 µM STS or 0.1% DMSO
182 control. Solid lines indicate population median, shaded areas indicate interquartile range.
183
184
185 ***Cellular profiling of phenylephrine-induced hypertrophy dynamics***

186 To examine hypertrophy dynamics with our high-content imaging assay, we stimulated
187 cardiomyocytes with the catecholamine phenylephrine (PE), an □1-adrenergic agonist and a
188 well-known inducer of cardiomyocyte hypertrophy [42], [43]. Cardiac □1-adrenergic signaling
189 has also been shown to activate cell survival signaling pathways [32], [44]. We further examined
190 the protein translation inhibitor cycloheximide (CHX) as an additional negative control to
191 control for baseline protein synthesis [45].

192 Treatment with PE increased two established metrics of hypertrophy: an increase in cell area
193 and hypertrophy and eGFP expression (**Figure 3A-C**). We previously found PE-induced
194 increase in cardiomyocyte 2D cell area to strongly correlate with 3D cell volume [43], and eGFP
195 expression driven by a constitutive promoter reflects overall protein synthesis. The greatest
196 increase in median cell areas relative to DMSO occurred around 24 h (**Figure 3D**).
197 Interestingly, there was substantial single-cell variability in PE-induced changes in cell area.
198 Comparison of the empirical cumulative distribution functions (eCDFs) of the DMSO- and PE-
199 treated cells show not simply a rightward shift in distribution when cells are treated with a
200 hypertrophic agonist, but rather an increase in the upper tail of distribution of cell areas
201 (**Figure 3F**). This indicates that population-level increases in cell area seen with PE treatment
202 are due to a subpopulation of hypertrophic responders as opposed to global increases in cell
203 area. PE treatment increased the proportion of hypertrophic responders, or cells with fold

change areas greater than that of the 75th percentile of DMSO, while CHX treatment reduced this proportion (**Figure 3G**). Cells treated with PE are shown in **Supplemental Movie 3** with increases in cell area and GFP expression on the single-cell level.

We previously identified divergent characteristics of cellular hypertrophy induced by different hypertrophic agonists [46]. While our previous approach segmented cells based on □-actinin immunofluorescence, here we found greater fidelity when further incorporating cell-to-cell variation in eGFP expression (**Supplemental Figure 2**). We therefore re-characterized the same metrics of cell shape and size and found that treatment with PE led to significant changes to all metrics observed (**Figure 3H**). As expected, PE increased raw cell area and major axis length. Elongation (axis ratio), eccentricity, and form factor all decreased, indicating PE-treated cells became more circular but more spiky (**Figure 3A**, red outline).

Previous reports have suggested a role for increased DNA synthesis and polyploidy in cardiac hypertrophy, and we recently published a method for determining cardiomyocyte nuclear ploidy with the nuclear stain DAPI [47], [48]. Further, Hoechst has been shown to be a reliable marker for chromatin condensation, which may play a functional role in transcription [49]. We therefore asked whether the hypertrophic stimulus PE also affected nuclear characteristics as measured by Hoechst. While nuclear morphological characteristics remained unchanged, Hoechst MAD was decreased, indicating altered chromatin condensation. We found that PE-treated cells initially took up less Hoechst than DMSO-treated counterparts but finished with an overall brighter Hoechst signal, indicating increased DNA content (**Figure 3I**). The smaller initial Hoechst intensity may reflect more robust nuclear membrane integrity due to the cell survival signaling pathways activated by PE and the relative rates of phospholipid turnover and DNA synthesis [50], [51]. Overall, these results show that PE induces both cardiomyocyte size but also metrics indicative of nuclear integrity.

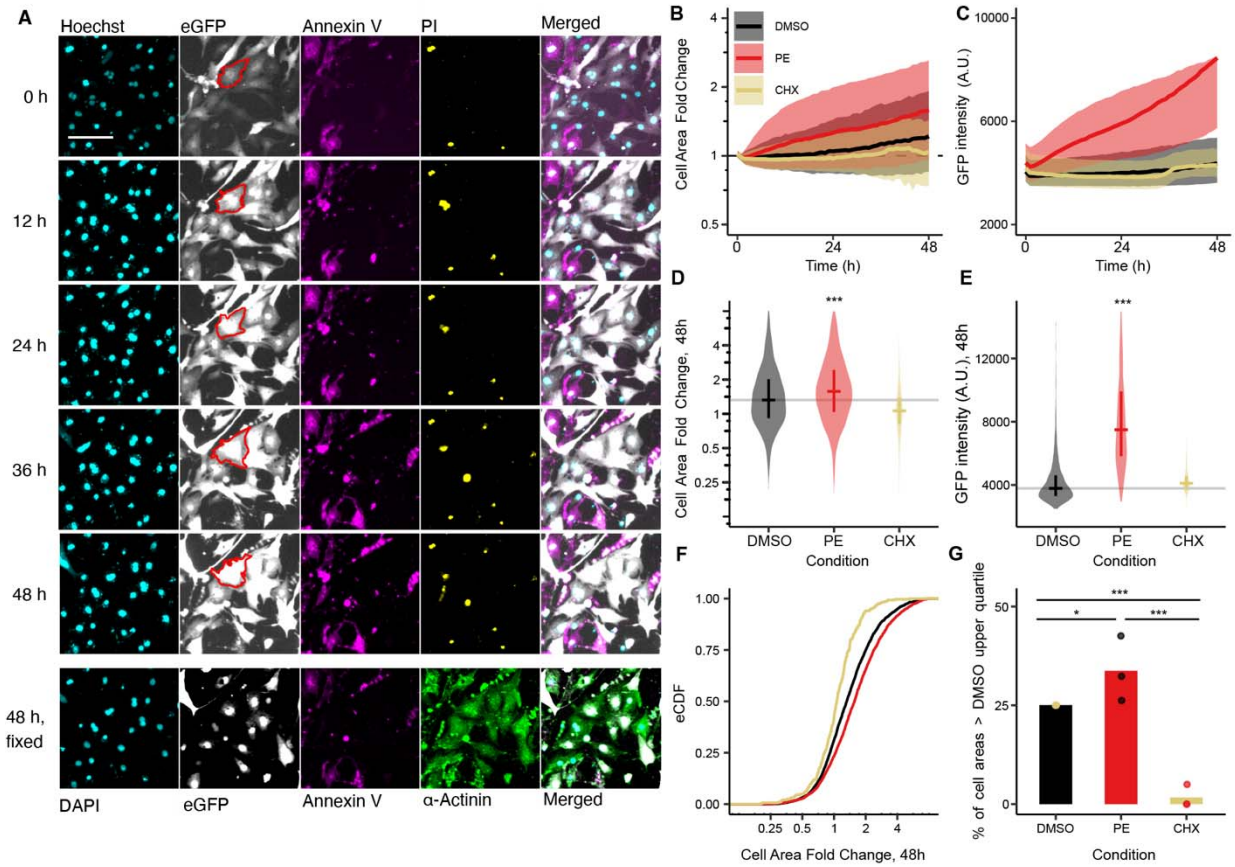
A
Hoechst
eGFP
Annexin V
PI
Merged
0 h
12 h
24 h
36 h
48 h
48 h, fixed
DAPI
eGFP
Annexin V
α-Actinin
Merged
B
DMSO
PE
CHX
Cell Area Fold Change
Time (h)
C
GFP intensity (A.U.)
Time (h)
D
Cell Area Fold Change, 48h
Condition
E
GFP intensity (A.U.), 48h
Condition
F
eCDF
Cell Area Fold Change, 48h
G
% of cell areas > DMSO upper quartile
Condition

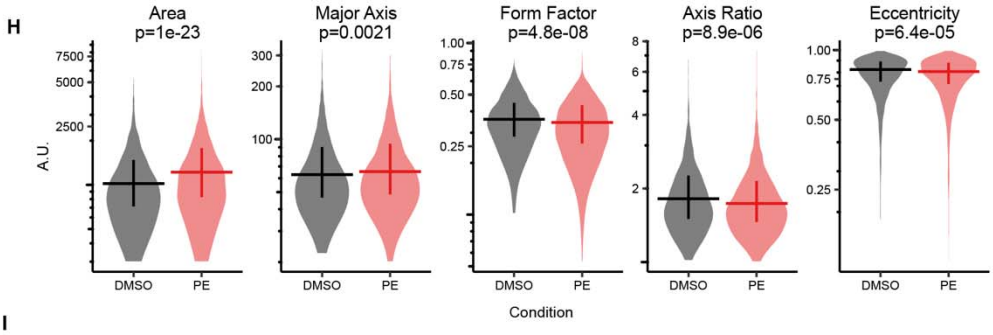
H
Area
p=1e-23
Major Axis
p=0.0021
Form Factor
p=4.8e-08
Axis Ratio
p=8.9e-06
Eccentricity
p=6.4e-05
A.U.
DMSO
PE
Condition

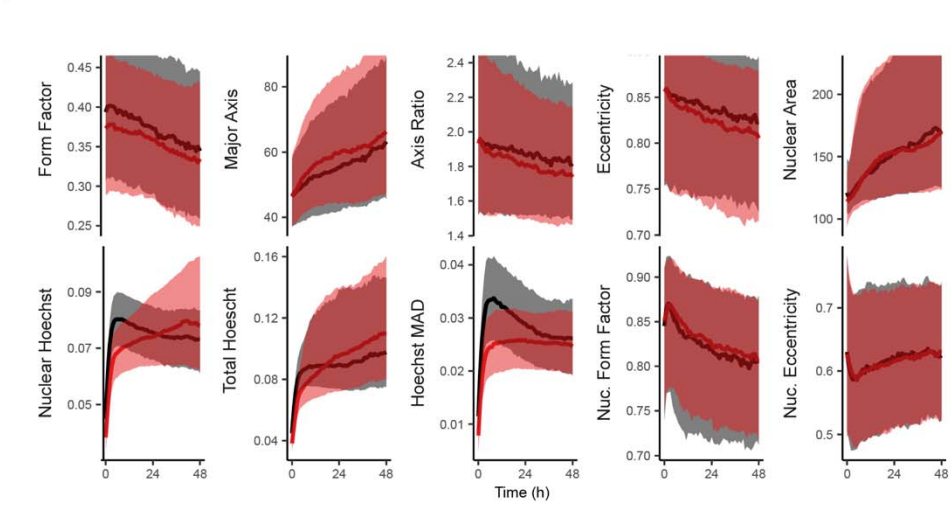
I
Form Factor
Major Axis
Axis Ratio
Eccentricity
Nuclear Area
Nuclear Hoechst
Total Hoescht
Hoechst MAD
Nuc. Form Factor
Nuc. Eccentricity
Time (h)

228

Figure 3. Phenylephrine induces coordinated changes in cell morphology, protein synthesis, and nuclear integrity.
(**A**) Representative timelapse images of neonatal rat cardiomyocytes treated with 50 µM PE showing induction of hypertrophy (red outline) and eGFP expression (gray).
48 h hypertrophy dynamics (**B**) and eGFP dynamics (**C**) of cells treated with 50 µM PE, 50 µM CHX, or 0.1% DMSO vehicle control. Solid lines indicate population median, shaded areas indicate interquartile range. 48 h treatment with 50µM PE induces hypertrophy (**D**) or eGFP expression (**E**). Errorbars indicate median and interquartile range *** $p < 2*10^{-16}$ *vs.* DMSO control, Kruskal–Wallis H test followed by one-sided Mann–Whitney U post-hoc test with Benjamini-Hochberg multiple testing correction, n = 2062-3416 cells.
(**F**) Empirical cumulative distribution functions (eCDFs) of cell areas. Same data as in (**D**).
(**G**) Percent of cells with areas greater than DMSO 75th percentile. Same data as in (**D**). *** $p \leq 1.58*10^{-6}$, mixed-effects ANOVA followed by Tukey HSD, 6 wells per condition for each of n = 3 independent cell isolations (represented as jitter points).
(**H**) Cell morphology metrics of cells treated with either 50 µM PE or 0.1% DMSO vehicle control at 48 h. Solid lines indicate population median, and error bars indicate interquartile range. p-values represent Kruskal–Wallis H test followed by one-sided Mann–Whitney U post-hoc test with Benjamini-Hochberg multiple testing correction, n = 2062-3416 cells.
(**I**) Single-cell dynamics of cellular or nuclear metrics in response to either 50 µM PE or 0.1% DMSO control. Solid lines indicate population median, shaded areas indicate interquartile range.

Isoproterenol induces biphasic dose-dependent hypertrophy and apoptosis dynamics

Computational models of the cardiomyocyte hypertrophy signaling network have identified A signaling as potentially both hypertrophic and apoptotic [8], [25]. The catecholamine isoproterenol (ISO) is a non-specific β-adrenergic receptor agonist and has been separately characterized as being either hypertrophic [30], [46], [52] or apoptotic [33], [53], [54]. Our assay provides a unique opportunity to investigate the dynamics of single-cell decision-making between these co-regulated hypertrophy and apoptosis [12], [27] that cannot be resolved by snapshots at individual timepoints.

To our knowledge, our assay shows for the first time the temporal dynamics of hypertrophy and apoptosis in the same cell population, in this case with ISO treatment (**Figure 4A**). ISO was previously shown to regulate cardiomyocyte contractility and hypertrophy with distinct

263 concentration dependence [52]. Therefore, we examined ISO responses over a 0.1-100 μM range
264 previously examined in studies of either cardiomyocyte hypertrophy or apoptosis [32], [33],
265 [52]. Interestingly, ISO induced a biphasic concentration-dependent hypertrophy response
266 (**Figure 4B** and **C**). While all ISO-treated conditions induced some level of hypertrophy relative
267 to the DMSO vehicle-treated control within 24 hours of treatment, medium to high doses of
268 isoproterenol (10 to 100 μM ISO) induced less hypertrophy or plateaued compared to lower
269 doses. This plateau was especially striking after 24 hours (**Figure 4D**), the timepoint associated
270 with apoptotic responses for STS stimuli. In contrast to the biphasic hypertrophy response, A5
271 binding showed an ultrasensitive response with enhanced apoptosis at very high ISO
272 concentrations (**Figure 4A**, **E**, and **F**) which are consistent with prior literature at the
273 population level. Previous studies with neonatal and adult rat cardiomyocytes have found that
274 ISO concentrations from 10 to 100 □M induce apoptosis as measured by cleavage of caspase 3
275 and PARP, TUNEL, DNA fragmentation, and regulation of ICER/Bcl2/Bad [33], [53], [55], [56],
276 [57]. Further, such studies have shown apoptosis induced by 10 to 100 μM ISO is prevented by
277 β-blockers and inhibitors of downstream protein kinase A, and L-type Ca^{2+} channels [33], [34],
278 [53], [58]. Furthermore, those experiments were generally conducted in serum-free cell growth
279 medium, which potentiate cells to undergo apoptosis [59], [60]. Consistent with previous
280 studies on fractional killing of cancer cell lines [28], we found that 100 μM ISO induced
281 substantial single-cell variability in growth and apoptosis (A5 binding of PI- cells) (**Figure 4G**).
282 Moreover, apoptotic cells were smaller at the time of A5 binding, denoted as “diers”, than their
283 A5- surviving counterparts, or “survivors” (**Figure 4H**), further demonstrating a relationship
284 between growth and death phenotypes.

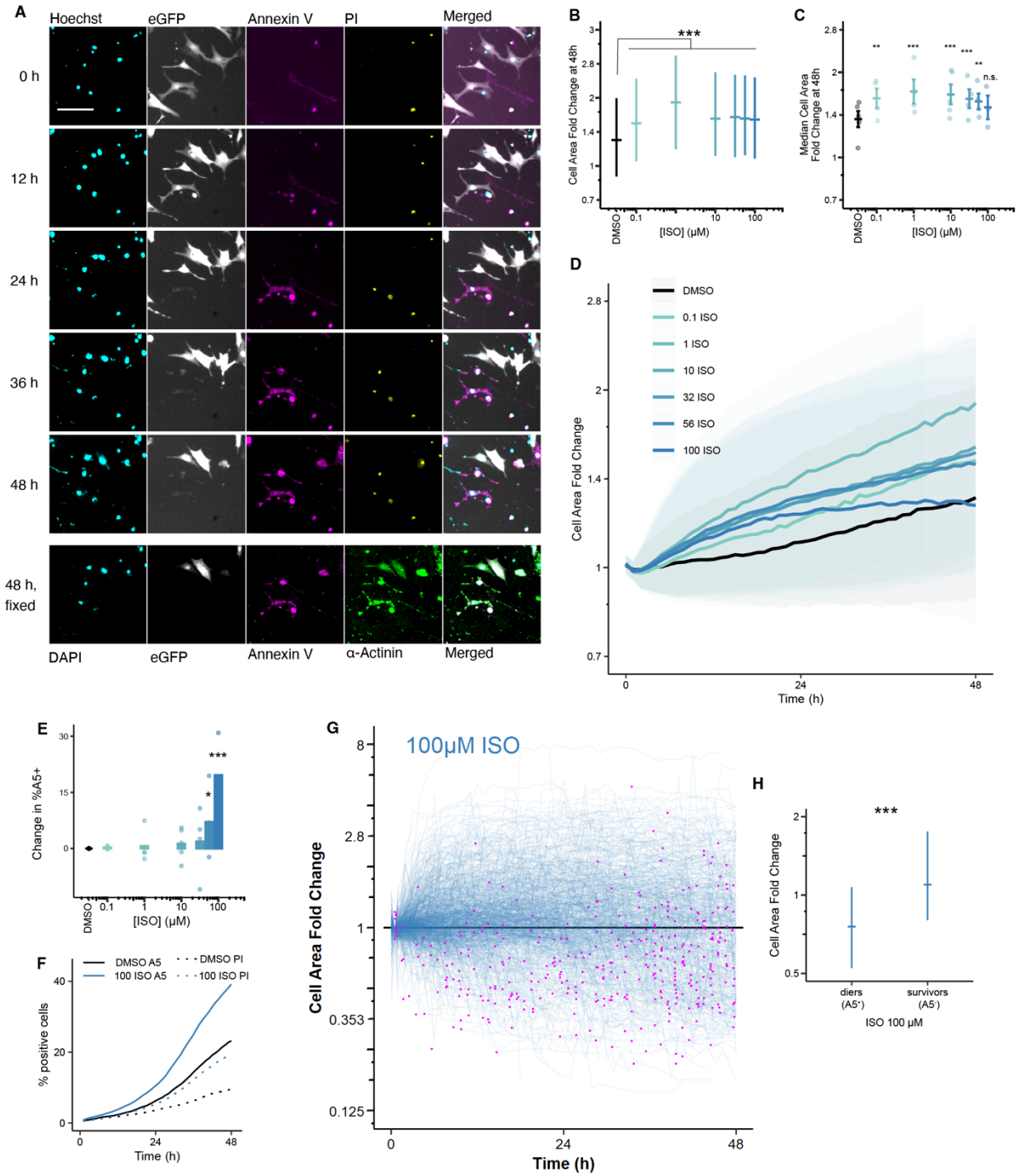

Figure 4. Isoproterenol stimulates distinct dose-dependent responses of hypertrophy and apoptosis, with substantial single-cell variability.
(**A**) Representative timelapse images of neonatal rat cardiomyocytes treated with 100 μM ISO showing induction of hypertrophy and A5 binding (magenta).
(**B**) Single-cell ISO concentration hypertrophy responses at 48 h. Solid lines indicate population median, errorbars indicate interquartile range. *** all ISO-treated conditions were significant

with $p \leq 2.22*10^{-16}$ *vs*. DMSO control; Kruskal–Wallis H test followed by one-sided Mann–Whitney U post-hoc test with Benjamini-Hochberg multiple testing correction, n = 4067-6780 cells.
(**C**) Median ISO concentration hypertrophy responses at 48 h across experiments. Error bars represent standard error of the mean. * $p < 0.05$, ** $p < 0.01$, *** $p < 0.001$; mixed effects ANOVA followed by one-sided Dunnett post hoc test, 6-9 wells per condition from each of n = 3-5 independent cell isolations.
(**D**) ISO concentration response of hypertrophy dynamics. Shaded area represents interquartile range.
(**E**) ISO concentration A5 binding response through 48 h. * $p < .05$, *** $p < .001$ vs DMSO control; mixed effects ANOVA followed by Dunnett post hoc test, same wells as in (**C**) with n = 3-5 independent cell isolations.
(**F**) Empirical cumulative distribution function of A5 (solid) and PI (dashed) binding for all cells treated either with DMSO or 100 µM ISO.
(**G**) Representative single-cardiomyocyte dynamic traces of morphology of cells treated with 100 µM ISO. Magenta dots indicate onset of A5 binding in PI- cardiomyocytes.
(**H**) Hypertrophy response of either area fold change at time of A5 binding (diers) or end of time course (survivors). Solid lines indicate population median, and error bars indicate interquartile range. *** $p < 2.2*10^{-16}$ *vs*. DMSO control, one-sided Mann-Whitney U test, n = 3268-5081 cells.

Differential response of cardiomyocyte subpopulations contributes to biphasic hypertrophy and ultrasensitive apoptosis

We hypothesized that the biphasic population-level responses to ISO may reflect heterogeneity in single-cell decision making between cell growth and death, with potential for functional crosstalk between these cell responses encompassed by three possible conceptual models that may be discriminated by multi-feature single-cell tracking (**Figure 5A**). To facilitate the comparison of cell hypertrophy and apoptosis, we first classified cells as “growers”, “stunned”, or “shrinkers”. Strikingly, the hypertrophic dynamics of these three subpopulations identified by single-cell tracking (**Figure 5B**) are qualitatively distinct from the transient population-level hypertrophic response to 100 µM ISO (**Figure 4B**). Thus, the transient population-level hypertrophy results from the early increases in the cell area of the “growers,” followed by the later decreased cell area of the “shrinkers,” and some cells remaining “stunned”. The “shrinker”

326 subpopulation was more prone to cell death and therefore contributed to the decrease in median
327 cell population area observed at later time points and higher ISO doses (**Figure 4E** and **H**).

328 As expected from the single-cell ISO concentration hypertrophy responses at 48 h, we saw a
329 trend towards an increased proportion of grower cells with ISO stimulation compared to DMSO.
330 In addition, the largest proportion of grower cells was seen with 1 μM ISO, which corresponds to
331 the dose at which we saw the greatest population-level hypertrophy response (**Figures 5C** and
332 **4C**, **D**). The relative decrease in the proportion of grower cells as ISO concentration is increased
333 beyond 10 μM ISO also correlated with the plateauing of the population-level hypertrophy ISO
334 concentration response (**Figure 4C** and **D**).

335 We hypothesized that growth and death responses may be discordant at the single-cell level,
336 with apoptosis primarily occurring in "shrinker" cells. We quantified the proportions of cells
337 from the three growth subpopulations that contribute to the ultrasensitive response of A5
338 binding with increasing ISO concentration (**Figure 5D**). At 100 μM ISO, shrinkers and stunned
339 cells were indeed statistically more likely than growers to become A5 positive, leading us to favor
340 a "grow-or-die" model over the "grow-and-die" model (**Figure 5E**). These concentration-
341 dependent hypertrophy and apoptosis decisions are quantified in state-transition diagrams that
342 are calculated directly from the proportion of cells in each state (**Figure 5F**). This
343 concentration-dependent hypertrophy and apoptotic states in ISO-treated cells are shown in
344 **Supplemental Movies 4 and 5**

345 Having found that apoptotic cells also tended to become smaller as "shrinkers" (**Figure 4H**),
346 we further analyzed the growth and death kinetics of the hypertrophic subpopulations to
347 determine additional causes for the biphasic hypertrophy concentration response observed at
348 the population level. Overall, cells that became A5 positive exhibited a median time lag from
349 maximal cell area to becoming A5 positive of 33 hours (**Figure 5G**). We next asked whether the
350 growth-death kinetics differed by hypertrophic subpopulation. Indeed, we found that stunned

351 cells grew to their maximal extent before 24 hours while growers continued growing after 24
352 hours (**Figure 5H**).

353 The three hypertrophic subpopulations further differed in their rate of apoptosis. The grower
354 and stunned subpopulations became A5+ 12 and 13 hours after reaching their maximal cell area,
355 respectively. Despite reaching maximal cell area early, the shrinker subpopulation persisted
356 longer with a median time lag of 19 hours before binding A5 (**Figure 5I**). From this analysis, we
357 conclude that the population-level biphasic hypertrophy in response to increasing ISO
358 concentration (**Figure 4D**) arose from multiple distinct subpopulations. The shrinker
359 subpopulation decreased in cell area and then underwent delayed apoptosis. In contrast, the
360 grower subpopulation increased in cell area with a reduced incidence of apoptosis. These
361 distinct subpopulation behaviors may represent an incoherent feedforward network motif
362 between -adrenergic receptor stimulation, hypertrophy, and apoptosis responsible for a single-
363 cell "grow-or-die" decision.

364 As a corollary to this "grow-or-die" conceptual model, we hypothesized that inhibiting the
365 apoptosis pathway may redirect cell decisions to the hypertrophy pathway. Under conditions of
366 100 μM ISO where we had found a mixed hypertrophy-apoptosis response, treatment with
367 caspase-3 inhibitor Z-DEVD-FMK [27] decreased cardiomyocyte apoptosis and the proportion
368 of shrinker cells while increasing the proportion of grower cells (**Supplemental Figure 3**).

369 We next asked whether, like ISO, PE-induced hypertrophy would also be protective from
370 apoptosis. As shown in **Supplemental Figure 4**, PE-treated growers were less likely to die
371 than shrinkers or stunned cells (**C**), and PE treatment increases the proportion of the grower
372 subpopulation compared to DMSO control (**D**). Thus, the "grow-or-die" conceptual model best
373 explains single-cell decisions in response to both ISO and PE stimulation.

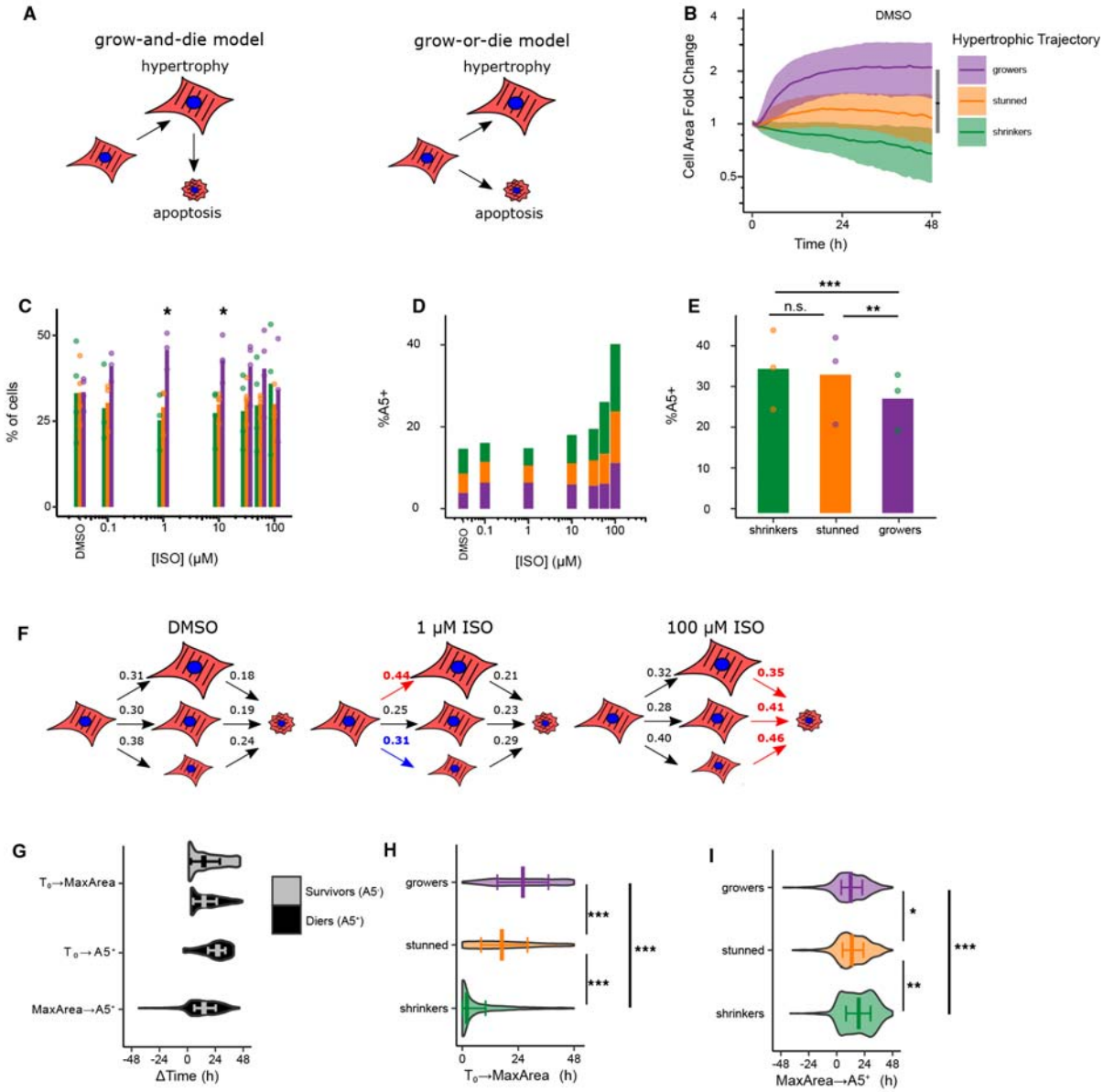

Figure 5. Single-cell hypertrophy-apoptosis tracking in response to isoproterenol supports a "grow-or-die" conceptual model.

All data is from experiments reported in Figure 4.

(**A**) Schematic of possible cardiomyocyte phenotypic decision-making models and relationships between hypertrophy and apoptosis.

(**B**) The population of cells treated with 100 μM ISO was partitioned into 3 hypertrophic trajectory groups relative to the DMSO-treated population at 48 h. Growers (purple) were defined as cells whose max fold change area was greater than that of the 75th percentile of the DMSO-treated population. Stunned (orange) cells were defined as cells whose max fold change area was in the DMSO-treated interquartile range. Shrinkers (green) were defined as cells whose max fold change area was less than the 25th percentile of the DMSO-treated cells. Solid lines indicate population median, shaded areas indicate interquartile range, black line indicates population median.

(**C**) 48-hour ISO concentration response of cell population makeup. Comparisons were made between each treatment's percent "grower" subpopulation. While the overall mixed-effects ANOVA was not statistically significant ($p = 0.094$) the more powered one-sided Dunnett's test showed statistically significant differences indicated with * $p < 0.05$ vs. DMSO control, 1-3 wells for each subpopulation per condition from $n = 3$-4 independent cell isolations. Moreover, the mixed-effects ANOVA between the 3 hypertrophy subpopulations was not significant for the DMSO treatment. However, there was a significant increase in the proportion of the grower subpopulation relative to the other two subpopulations with $p < 0.01$, mixed-effects ANOVA followed by Tukey HSD.
(**D**) Concentration response of cell growth subpopulation distribution for all apoptotic cells from **Figure 4E**.
(**E**) Cell population makeup for 100 µM ISO. Error bars represent mean ± SEM. ** $p = 0.00562$, *** $p < 0.001$, mixed-effects ANOVA followed by Tukey HSD, 1-3 wells per subpopulation from each of $n = 3$ independent cell isolations.
(**F**) Hypertrophy and apoptosis transition state diagrams for different ISO concentrations, derived from panel D as direct proportions of cells in each subpopulation. Red or blue arrows indicate an increase or decrease in transition probability of > 0.05 compared to DMSO, respectively.
(**G**) Single-cell quantification for 100 µM ISO, of onset of maximal hypertrophic area and A5 binding, and with the lag between those two events for cells that become A5+ (diers) or remain A5- (survivors).
For each hypertrophy subpopulation, we quantified time to maximal hypertrophy (**H**, n = 2378-3375 cells) or time between maximal hypertrophy and A5 binding (**I,** n = 824-1440 cells) as in **G**. Solid lines indicate population median, error bars indicate interquartile range. * $p = 0.017$, ** $p = 9.0*10^{-14}$, *** $p < 2*10^{-22}$, Kruskal–Wallis H test followed by Dunn's All-Pairs Rank Comparison post-hoc test with Benjamini-Hochberg multiple testing correction.

Initial cell morphology and nucleus predicts single-cell decisions of growth or death

Given the considerable single-cell heterogeneity in response to ISO stimulation, we asked whether pre-existing features of cardiomyocytes would predict their subsequent growth or death. We used a multinomial log-linear regression machine learning model to identify cellular features that may predict single-cell decisions of growth and/or death (**Methods, Figure 6A, Supplemental Table 1**). The response variable was one of 6 pairwise combinations of the 3 hypertrophic trajectory classifications and the binary survival/death outcome. The predictor variables were the 6 cellular and 6 nuclear size, shape, and fluorescence intensity features

425 identified by our assay as potentially relevant to cardiomyocyte apoptosis or hypertrophy
426 (**Figures 2** and **3**). 5-fold cross-validation repeated 100 times showed that the machine
427 learning model predicts the single-cell hypertrophy-apoptosis response to 100 μM ISO with an
428 accuracy of 32.2±0.1% (mean±SEM) and $R^2_{McFadden}$ of 0.075. This accuracy was similar to that of
429 a "random forest" model (accuracy of 32.7±0.1%, mean±SEM, **Supplemental Figure 5B**), but
430 the multinomial regression model approach provides value in the interpretability of the
431 coefficient values of each classifier. Both multinomial regression and random forest machine
432 learning models performed significantly better than the multinomial null model (accuracy of
433 20.8±0.01, mean±SEM). The similarity of accuracy in both approaches shows that differences in
434 model structure were less important than unmeasured initial features or sources of stochasticity.
435 The accuracy of all models was limited by substantial single-cell variability.

436 Analysis of the log-linear model identified several initial cell metrics that were predictive of
437 hypertrophy, apoptosis, or both. One such metric was the initial cell area - the model predicted
438 that initially larger cells had a higher likelihood of being stunned or shrinking and a lower
439 likelihood of growing (**Figure 6A**). The relationships identified in the model between initial cell
440 features and growth-death responses motivated further verification. Indeed, growers had an
441 initial cell size that was smaller than shrinker or stunned subpopulations (**Figure 6B**). Analysis
442 of the growth trajectory of cells in either the bottom or top quartiles of initial cell area
443 distributions also showed that small cells had a hypertrophic growth response while larger cells
444 did not hypertrophy significantly (**Figure 6C**). While the initial area regression coefficient did
445 not specifically correlate with the survival status of a cell, it had an especially strong statistical
446 association with the shrinker/dier population. Indeed, cells in the largest quartile of initial cell
447 areas were more likely to die than those in the smallest quartile (**Figure 6D**). A parallel random
448 forest regression model showed that the initial area was the most influential metric for model
449 accuracy (**Supplemental Figure 5C**). Cells with small initial area were also less likely to
450 apoptose in response to PE treatment (**Supplementary Figure 4D**). These initial cell size-

451 dependent hypertrophy and apoptosis decisions are summarized in **Figure 6F,** where large
452 cells are more likely to shrink and die. Our data show that with both ISO and PE treatment,
453 hypertrophic signaling confers partial protection against apoptosis. Thus, our analysis of single-
454 cell predictors of growth/death decisions further supports the "grow-or-die" model over the
455 "grow-and-die" model.

456 Interestingly, this analysis identified nuclear Hoechst intensity (reflecting DNA content or
457 nuclear permeability) and its median absolute deviation (reflecting chromatin condensation) as
458 two nuclear metrics predictive of both cell growth and survival (**Figure 6A**). The median
459 absolute deviation metric was also implicated as the second most influential metric for model
460 accuracy by the random forest model (**Supplemental Figure 5C**). Similarly, our single-cell
461 chromatin as measured by Hoechst MAD compared to cells in all other subpopulations (**Figure**
462 **6E**), which we also observed in our PE- and 56 μM ISO-treated cells at the population level
463 (**Figure 3I** and **Supplemental Figure 1**).

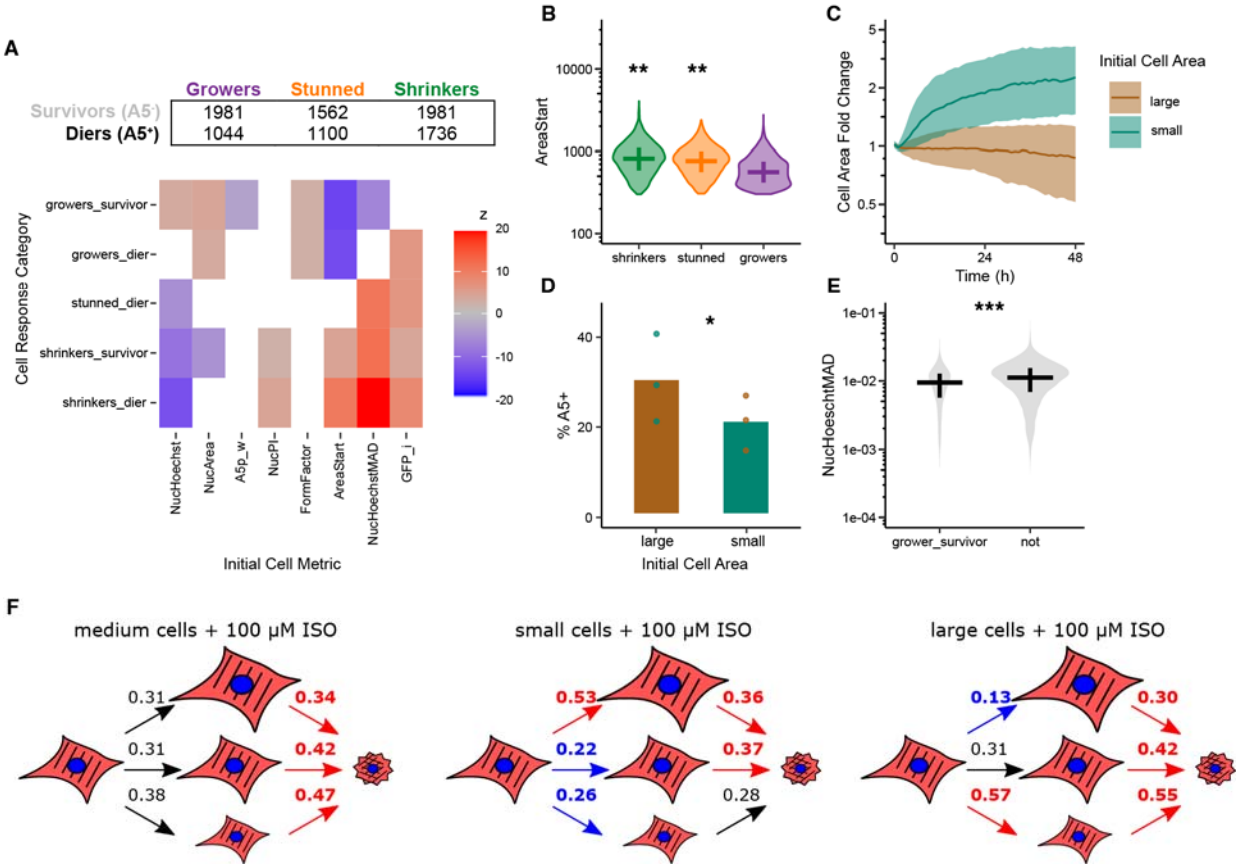

Figure 6. Multinomial log-linear model reveals initial cell features that predict single-cell hypertrophy-apoptosis decisions in cardiomyocytes treated with 100 μM ISO.

All data is from experiments reported in Figure 4.

(**A**) Significant multinomial log-linear model coefficient z-scores. The contingency table contains the number of cells in each hypertrophy-death category. The model self-validates with an accuracy of 33.26% ($R^2_{McFadden}$ = 0.075), with a 5-fold cross-validation accuracy of 32.33+/-0.01% (n = 100 permutations) (**Supplemental Figure 5)**.

(**B**) Initial cell areas of each hypertrophic trajectory group. Solid lines indicate population median, error bars indicate interquartile range. ** p ≤ 2*10-16 vs. grower population, Kruskal–Wallis H test followed by one-sided Mann–Whitney U post-hoc test with Benjamini-Hochberg multiple testing correction, n = 2662-3738 cells.

(**C**) 48h hypertrophy dynamics of cells in either the bottom or top quartile of the initial cell area. Solid lines indicate population median, shaded areas indicate interquartile range.

(D) 48h total A5 binding of cells in either the bottom or top quartile of the initial cell area. * p = 0.027, one-sided Welch's paired T-test, 1-3 wells per condition from each of n = 3 independent cell isolations.

(E) Initial nuclear Hoechst MAD of grower-survivor group vs. all other cells. Solid lines indicate population median, error bars indicate interquartile range. *** p = 2.4*10^-36, one-sided Mann-Whitney U test, n = 1981-7444 cells.

(F) Hypertrophy and apoptosis transition state diagrams for different cardiomyocyte subpopulations. Arrow colors are relative to the DMSO diagram in **Figure 5F**, with red or blue indicating an increase or decrease in transition probability of > 0.05.

Discussion

Single-cell, multiplexed, or longitudinal data each have the potential for elucidating new causal relationships or differential cell responses to stimuli [61], [62], [63]. Most recently, single-cell and single-nucleus RNA sequencing (scRNA-seq and snRNA-seq) have identified new cardiac cell subpopulations and single-cell specific mechanisms that contribute to heart failure [24], [64], [65]. We still do not fully understand the role of functional diversity among cardiac cell types in disease progression, but recent advances in sequencing have illustrated importance in assessing cellular heterogeneity in both the healthy and failing heart.

Expression of the fetal gene program is a common surrogate for cardiomyocyte hypertrophy measurements [66], [67], but bulk measurements capture neither the changes in cell morphology nor heterogeneity of single-cell behaviors. Fixed cell cytometry approaches may capture phenotypic endpoints but lack information about the initial system state or the phenotypic trajectories necessary to elucidate decision-making processes without the use of additional system perturbations [27], [63], [68]. Previous studies of single-cell decision-making have largely been in non-myocytes and have examined decision-making for a single phenotype [28], [69], [70]. Here, our high-content microscopy platform extends previous work on automated live imaging of single-cell hypertrophy to address the challenges of measuring single-cell hypertrophy and apoptosis simultaneously. This study leveraged simple genetically encoded and biochemical fluorescent reporters to track morphological and biochemical dynamics in single cells necessary to investigate fundamental cell decisions of growth and death.

After validating our cardiomyocyte assay for hypertrophy and apoptosis measurements separately and identifying new features of those processes, we used our assay to examine the

510 dynamics of decision-making between hypertrophy and apoptosis in response to
511 catecholamines. Theoretical mechanisms underlying the simultaneous regulation of analog and
512 digital phenotypic decision-making by a single signaling network have been proposed. To our
513 knowledge, however, the relative timing of early analog hypertrophy responses and late digital
514 apoptosis decisions represents the first experimental support of a single signaling network
515 regulating a mixture of analog and digital phenotypic decisions [71]. Leveraging these
516 heterogeneity dynamics in our cell populations, we identified a biphasic hypertrophic ISO
517 concentration response at the cell-population level, implying at least two underlying, competing
518 processes. We therefore hypothesized that different subpopulations of cells contribute to the
519 overall population response.

520 Our data with both ISO and PE treatment best supports a "grow or die" conceptual model in
521 which hypertrophic signaling is moderately protective against apoptosis. The transition-state
522 diagrams show that while all three subpopulations undergo apoptosis at high-dose ISO
523 treatment, the grower subpopulation is more resistant to undergo apoptosis compared to the
524 shrinker subpopulation. Likewise, the PE-treated grower subpopulation had a decreased
525 incidence of apoptosis. However, at low-dose ISO treatment, there is an increase in the grower
526 subpopulation and a decrease in the shrinker subpopulation without any increase in apoptosis
527 between those populations. Further, inhibiting caspase 3 activity re-routed cardiomyocytes from
528 apoptosis to hypertrophy. Together, these observations of differential apoptosis among
529 hypertrophic subpopulations undermine the "grow-and-die" model and in favor of the "grow-or-
530 die" model under both ISO and PE treatment.

531 We used cyclic data-driven hypothesis testing and modeling to identify characteristic features of
532 these different subpopulations. Our multinomial log-linear regression models sought to identify
533 nongenetic heterogeneities in initial cell size, morphology, and fluorescence metrics at a single
534 ISO dose that would predict dynamic, single-cell decision-making. This modeling approach had

535 an accuracy rate similar to the more agnostic, black-box “random forest” model. This shows that
536 differences in model structure (such as the presence of non-linear interactions between
537 predictors) were less important than other, non-characterized factors or biochemical sources of
538 stochasticity[72], [73]. Even so, we identified and validated a smaller initial cell size as
539 predictive of greater hypertrophy and survival. Surprisingly, we identified two nuclear metrics,
540 DNA intensity (integrated Hoeschst), and chromatin heterogeneity (Hoechst MAD), that
541 predicted cell hypertrophy and survival, which implies a potential role for transcriptional
542 regulation of differential cell decision-making between growth and death [74], [75]. These three
543 metrics were also predictive of hypertrophy/apoptosis decision-making with other treatments,
544 namely PE and other ISO concentrations. The caspase inhibitor Z-DEVD-FMK decreased the
545 “shrinker” subpopulation and increased the “grower” subpopulation, indicating that decisions
546 toward death can be prevented.

547 We envision multiple avenues for extending the approach presented herein. We focused on
548 neonatal cardiomyocytes for their feasibility of 48 hr tracking, de-differentiation/death of adult
549 cardiomyocytes, and because substantial literature supports overall similarities with adult cells
550 in hypertrophy-apoptosis [33], [53], [54], [58]. However, there are also well-known differences
551 with maturation, in which adult cells may be more predictive on in vivo decision-making.
552 Tracking *in vitro* co-culture models of cardiomyocytes and fibroblasts and the relative local
553 density of those cells would provide new insight into paracrine signaling interactions between
554 cardiomyocytes and fibroblasts to yield new potential therapeutic targets [76]. Additional
555 phenotypes such as cardiomyocyte proliferation could also multiplexed with our assay to
556 examine additional single-cell decisions [48]. Our fluorescent reporter could be replaced with
557 reporters of signaling pathway activity to provide mechanistic insight into cellular decision-
558 making [77]. Can these decisions be tracked in vivo? Single-cell RNA-sequencing can identify
559 sub-populations but not resolve the dynamic decision making. Light-sheet microscopy of live
560 zebrafish has enabled testing of hypotheses previously limited to cell culture [78], [79], although

these approaches have not typically had fully automated cell analysis and are less relevant to hypertrophy-apoptosis in mammalian hearts. Alternatively, the current study may motivate sophisticated dual-color lineage tracing [80] to test the “grow-or-die” conceptual model in vivo. Overall, the high-content live-cell microscopy approach presented here provides an improved understanding of cellular multi-tasking in response to stress.

Funding

This work was funded by the National Institutes of Health (BC: HL134266, GM007267, GM008715; JJS: HL13775, HL137100; OD021723) and National Science Foundation (1252854).

Acknowledgements

We thank members of the Saucerman lab, including B. Wissmann for technical support with cardiomyocyte isolations, P. Tan for support with CellProfiler, and L. Woo for discussions and providing feedback on this work. We also thank Chris Smolko and Kevin Janes for contributing to the eGFP lentivirus. We acknowledge Research Computing at The University of Virginia for providing computational resources and technical support.

Author contributions

Conceptualization, B.C. and J.J.S.; Methodology, B.C., L.N. and J.J.S.; Investigation, B.C., L.N. and J.J.S.; Writing, B.C. and J.J.S.; Funding Acquisition, J.J.S.; Supervision, J.J.S..

578 # Methods

579 ***Chemical Reagents***

580 - DMSO (R&D Systems, Cat#3176)
581 - Staurosporine (R&D Systems, Cat#1285)
582 - (R)-(-)-Phenylephrine hydrochloride (R&D Systems, Cat#2838)
583 - Isoproterenol hydrochloride (R&D systems, Cat#1747)
584 - Z-DEVD-FMK (R&D Systems, Cat#2166)

585 ***Lentivirus***

586 Lentiviruses were prepared in 293T/17 cells (ATCC) by triple transfection with psPAX2,
587 pMD.2G, and PLX302 eGFP as previously described [81], [82]. The plasmids were a gift from K.
588 Janes (University of Virginia).

589 ***Cell Culture***

590 Cardiac myocytes were harvested from 1–2 day-old Sprague-Dawley rats using the Neomyts
591 isolation kit (Cellutron, Baltimore, MD). All procedures were performed in accordance with the
592 Guide for the Care and Use of Laboratory Animals published by the U.S. National Institutes of
593 Health and approved by the University of Virginia Institutional Animal Care and Use
594 Committee. Myocytes were cultured in plating media (Dulbecco's modified Eagle media
595 supplemented with 17% M199, 10% horse serum(Gibco, 16050122), 5% fetal bovine serum
596 (HyClone FBS Thermo Scientific Cat: SH30396.03 Lot: AUD34652), 50 U/mL penicillin, 50
597 µg/mL streptomycin (Gibco, 15140122), 4.8mM L-glutamine(Gibco, 25030081) at a density of
598 20,000 cells per well of a 96-well CellBIND plate (Corning) coated with SureCoat (Cellutron).

599 Cells were transduced with 100µL of eGFP lentivirus and plating media supplemented with
600 8µg/mL polybrene (Santa Cruz Biotechnology, Cat#sc-134220) at the time of plating and after
601 24 hours. Cells were contractile at the time of transduction. 36 hours after plating, the medium
602 was replaced with low-serum media (phenol-red free Dulbecco's modified Eagle media
603 supplemented with 17% M199, 0.1% FBS, 1% ITSS, 20mM HEPES, 50 U/mL penicillin, 50
604 µg/mL streptomycin, 4.8 mM L-glutamine) for 24 hours of serum starvation prior to treatment.

605 ***Dual hypertrophy/apoptosis assay***

606 Cells were pre-stained and pre-treated with relevant small molecule inhibitors in low-serum
607 media supplemented with 27 nM Hoechst 33342, 0.5 nM Propidium iodide, and 0.5× Alexa
608 Fluor 647–conjugated A5 (Invitrogen) for 2 hours. Cells were imaged on the Operetta CLS high-
609 content imaging system (Perkin-Elmer) using a 10×□0.3NA objective in widefield mode, which
610 integrates over the entire cell thickness. Temperature and CO2 control options were set to 37°C
611 and 5% CO2, respectively. Images were captured every 1 hour for 48 hours. 4 fields of view were
612 acquired for each well.

613 After live-cell imaging, the cells were fixed with 4% PFA and stained with DAPI and monoclonal
614 anti-α-Actinin antibody (Sigma, Cat#A7811). The same fields of view acquired during live
615 imaging were again imaged.

616 ***Image Processing***

617 All images were processed using Matlab 2018a (MathWorks), ilastik[78], and CellProfiler[79].
618 Images were flat-field corrected in Matlab using reference dark field and flat-field images taken
619 of fluorescence reference slides (Ted Pella). Corrected fluorescence signals from GFP, A5, and α-
620 Actinin images were converted to probability maps using the pixel classification tool in ilastik
621 [83].

An image analysis pipeline was developed in CellProfiler to automatically segment, measure, and classify the cells from the corrected images and signal probability maps. Briefly, all live timepoints and fixed immunofluorescence images were aligned to the final timepoint images. Hoechst- and propidium iodide-positive nuclei were independently segmented using Otsu thresholding. Binucleates were identified by merging touching nuclei and then shrunken by a radius of 1 pixel. GFP positive cells were identified using a watershed segmentation algorithm on the GFP probability map using the merged nuclei as starting seeds. These GFP positive cells were tracked and measured for morphological and fluorescence intensity characteristics including area, GFP intensity, A5 intensity and probability, final α-Actinin intensity and probability. Nuclei were also measured for morphological and propidium iodide and Hoechst intensities.

Statistical Analysis

All statistical analyses were done in R version 3.6.3. The following packages were additionally used for general data preparation and visualization: tidyverse [84], multcomp [85], nlme [86], nnet [87], perturb [88], PMCMRplus [89] , randomForest [90], stargazer [91] and tableplot [92]. Comparisons of single cell level metrics were performed as n = cells. Comparisons of population-level statistics were performed as n = independent cell isolations, generally with a mixed effects ANOVA with appropriate post-hoc tests. In situations in which the ANOVA was not significant but there was a predefined hypothesis, post-hoc analysis was still conducted as recommended [93]. Mixed effects ANOVA with independent cell isolations were modeled as a random effect.

Modeling

Data were normalized prior to statistical modeling. For multinomial log-linear modelling, predictor variables were filtered for multicollinearity on the basis of their variance inflation

factor (VIF) scores - removal of the raw major axis length metric reduced all VIF scores below a maximum of 2.4. We also verified the remaining collinearities with a tableplot and that those variables described sufficiently different metrics (**Supplemental Figure 5A**). For random forest modelling, default values from the randomForest package were used with the exception of 1000 trees [90].

References

[1] C. Nüsslein-Volhard and E. Wieschaus, “Mutations affecting segment number and polarity in Drosophila,” *Nature*, vol. 287, no. 5785, pp. 795–801, Oct. 1980, doi: 10.1038/287795a0.

[2] M. D. Petkova, G. Tkačik, W. Bialek, E. F. Wieschaus, and T. Gregor, “Optimal Decoding of Cellular Identities in a Genetic Network,” *Cell*, vol. 176, no. 4, pp. 844-855.e15, Feb. 2019, doi: 10.1016/j.cell.2019.01.007.

[3] M. Behar, H. G. Dohlman, and T. C. Elston, “Kinetic insulation as an effective mechanism for achieving pathway specificity in intracellular signaling networks,” *Proc Natl Acad Sci U S A*, vol. 104, no. 41, pp. 16146–16151, Oct. 2007, doi: 10.1073/pnas.0703894104.

[4] M. Behar, D. Barken, S. L. Werner, and A. Hoffmann, “The dynamics of signaling as a pharmacological target,” *Cell*, vol. 155, no. 2, pp. 448–461, Oct. 2013, doi: 10.1016/j.cell.2013.09.018.

[5] J. J. Saucerman and A. D. McCulloch, “Cardiac beta-adrenergic signaling: from subcellular microdomains to heart failure,” *Ann N Y Acad Sci*, vol. 1080, pp. 348–61, Oct. 2006, doi: 1080/1/348.

[6] N. Frey, H. A. Katus, E. N. Olson, and J. A. Hill, “Hypertrophy of the heart: a new therapeutic target?,” *Circulation*, vol. 109, no. 13, pp. 1580–1589, Apr. 2004, doi: 10.1161/01.CIR.0000120390.68287.BB.

[7] D. Levy, R. J. Garrison, D. D. Savage, W. B. Kannel, and W. P. Castelli, “Prognostic implications of echocardiographically determined left ventricular mass in the Framingham Heart Study,” *N Engl J Med*, vol. 322, no. 22, pp. 1561–1566, May 1990, doi: 10.1056/NEJM199005313222203.

[8] K. Ryall, D. Holland, K. Delaney, M. Kraeutler, A. Parker, and J. Saucerman, “Network reconstruction and systems analysis of cardiac myocyte hypertrophy signaling.,” *The Journal of biological chemistry*, vol. 287, no. 50, pp. 42259–42268, Dec. 2012, doi: 10.1074/jbc.m112.382937.

[9] D. Wencker *et al.*, “A mechanistic role for cardiac myocyte apoptosis in heart failure,” *J. Clin. Invest.*, vol. 111, no. 10, pp. 1497–1504, May 2003, doi: 10.1172/JCI17664.

[10] G. W. Dorn, “The Fuzzy Logic of Physiological Cardiac Hypertrophy,” *Hypertension*, vol. 49, no. 5, pp. 962–970, May 2007, doi: 10.1161/HYPERTENSIONAHA.106.079426.

[11] M. Sano *et al.*, “p53-induced inhibition of Hif-1 causes cardiac dysfunction during pressure overload,” *Nature*, vol. 446, no. 7134, pp. 444–448, Mar. 2007, doi: 10.1038/nature05602.

[12] V. P. van Empel and L. J. De Windt, “Myocyte hypertrophy and apoptosis: a balancing act,” *Cardiovascular research*, vol. 63, no. 3, pp. 487–499, 2004.

[13] D. D. D'Angelo *et al.*, "Transgenic Gαq overexpression induces cardiac contractile failure in mice," *Proc. Natl. Acad. Sci. U.S.A.*, vol. 94, no. 15, pp. 8121–8126, Jul. 1997, doi: 10.1073/pnas.94.15.8121.

[14] W. Grossman, D. Jones, and L. McLaurin, "Wall stress and patterns of hypertrophy in the human left ventricle.," *The Journal of clinical investigation*, vol. 56, no. 1, pp. 56–64, Jul. 1975, doi: 10.1172/jci108079.

[15] Y. Hayakawa *et al.*, "Inhibition of Cardiac Myocyte Apoptosis Improves Cardiac Function and Abolishes Mortality in the Peripartum Cardiomyopathy of Gαq Transgenic Mice," *Circulation*, vol. 108, no. 24, pp. 3036–3041, Dec. 2003, doi: 10.1161/01.CIR.0000101920.72665.58.

[16] J. Owens, "Better beta-blockers," *Nat Rev Drug Discov*, vol. 4, no. 5, pp. 371–371, May 2005, doi: 10.1038/nrd1713.

[17] S. Engelhardt, L. Hein, F. Wiesmann, and M. J. Lohse, "Progressive hypertrophy and heart failure in β_1-adrenergic receptor transgenic mice," *Proc. Natl. Acad. Sci. U.S.A.*, vol. 96, no. 12, pp. 7059–7064, Jun. 1999, doi: 10.1073/pnas.96.12.7059.

[18] E. Teiger *et al.*, "Apoptosis in pressure overload-induced heart hypertrophy in the rat.," *The Journal of clinical investigation*, vol. 97, no. 12, pp. 2891–2897, 1996.

[19] Y. Shizukuda, P. M. Buttrick, D. L. Geenen, A. C. Borczuk, R. N. Kitsis, and E. H. Sonnenblick, "β-Adrenergic stimulation causes cardiocyte apoptosis: influence of tachycardia and hypertrophy," *American Journal of Physiology-Heart and Circulatory Physiology*, vol. 275, no. 3, pp. H961–H968, Sep. 1998, doi: 10.1152/ajpheart.1998.275.3.H961.

[20] L. J. De Windt *et al.*, "Calcineurin-Mediated Hypertrophy Protects Cardiomyocytes From Apoptosis In Vitro and In Vivo: An Apoptosis-Independent Model of Dilated Heart Failure," *Circulation Research*, vol. 86, no. 3, pp. 255–263, Feb. 2000, doi: 10.1161/01.RES.86.3.255.

[21] J. E. Springer, R. D. Azbill, S. A. Nottingham, and S. E. Kennedy, "Calcineurin-mediated BAD dephosphorylation activates the caspase-3 apoptotic cascade in traumatic spinal cord injury," *Journal of Neuroscience*, vol. 20, no. 19, pp. 7246–7251, 2000.

[22] H.-G. Wang *et al.*, "Ca^{2+}-Induced Apoptosis Through Calcineurin Dephosphorylation of BAD," *Science*, vol. 284, no. 5412, pp. 339–343, Apr. 1999, doi: 10.1126/science.284.5412.339.

[23] E. C. Greenwald, J. M. Redden, K. L. Dodge-Kafka, and J. J. Saucerman, "Scaffold state switching amplifies, accelerates, and insulates protein kinase C signaling," *J Biol Chem*, vol. 289, no. 4, pp. 2353–2360, Jan. 2014, doi: 10.1074/jbc.M113.497941.

[24] M. Chaffin *et al.*, "Single-nucleus profiling of human dilated and hypertrophic cardiomyopathy," *Nature*, vol. 608, no. 7921, pp. 174–180, Aug. 2022, doi: 10.1038/s41586-022-04817-8.

[25] J. Kang, H.-S. Lee, Y.-W. Kang, and K.-H. Cho, "Systems biological approaches to the cardiac signaling network," *Briefings in Bioinformatics*, p. bbv039, Jun. 2015, doi: 10.1093/bib/bbv039.

[26] D. B. Sawyer, D. A. Siwik, L. Xiao, D. R. Pimentel, K. Singh, and W. S. Colucci, "Role of oxidative stress in myocardial hypertrophy and failure," *Journal of molecular and cellular cardiology*, vol. 34, no. 4, pp. 379–388, 2002.

[27] C. Putinski *et al.*, "Intrinsic-mediated caspase activation is essential for cardiomyocyte hypertrophy.," *Proceedings of the National Academy of Sciences of the United States of America*, vol. 110, no. 43, pp. E4079–E4087, Oct. 2013, doi: 10.1073/pnas.1315587110.

[28] J. Roux *et al.*, "Fractional killing arises from cell□to□cell variability in overcoming a caspase activity threshold," *Molecular Systems Biology*, vol. 11, no. 5, p. 803, May 2015, doi: 10.15252/msb.20145584.

[29] C. Morisco, D. C. Zebrowski, D. E. Vatner, S. F. Vatner, and J. Sadoshima, “β-Adrenergic cardiac hypertrophy is mediated primarily by the β1-subtype in the rat heart,” *Journal of molecular and cellular cardiology*, vol. 33, no. 3, pp. 561–573, 2001.
[30] K. A. Ryall, V. J. Bezzerides, A. Rosenzweig, and J. J. Saucerman, “Phenotypic screen quantifying differential regulation of cardiac myocyte hypertrophy identifies CITED4 regulation of myocyte elongation,” *Journal of molecular and cellular cardiology*, vol. 72, pp. 74–84, 2014.
[31] M. Vidal, T. Wieland, M. Lohse, and K. Lorenz, “β-Adrenergic receptor stimulation causes cardiac hypertrophy via a Gβγ/Erk-dependent pathway,” *Cardiovascular Research*, vol. 96, no. 2, pp. 255–264, Nov. 2012, doi: 10.1093/cvr/cvs249.
[32] E. Iwai-Kanai, K. Hasegawa, M. Araki, T. Kakita, T. Morimoto, and S. Sasayama, “alpha- and beta-adrenergic pathways differentially regulate cell type-specific apoptosis in rat cardiac myocytes,” *Circulation*, vol. 100, no. 3, pp. 305–311, Jul. 1999, doi: 10.1161/01.cir.100.3.305.
[33] S. Saito *et al.*, “β-Adrenergic pathway induces apoptosis through calcineurin activation in cardiac myocytes,” *Journal of Biological Chemistry*, vol. 275, no. 44, pp. 34528–34533, 2000.
[34] S.-Y. Shin *et al.*, “The switching role of β-adrenergic receptor signalling in cell survival or death decision of cardiomyocytes,” *Nature Communications*, vol. 5, p. 5777, Dec. 2014, doi: 10.1038/ncomms6777.
[35] F. Meggio *et al.*, “Different Susceptibility of Protein Kinases to Staurosporine Inhibition: Kinetic Studies and Molecular Bases for the Resistance of Protein Kinase CK2,” *European Journal of Biochemistry*, vol. 234, no. 1, pp. 317–322, Nov. 1995, doi: 10.1111/j.1432-1033.1995.317_c.x.
[36] C. A. Belmokhtar, J. Hillion, and E. Ségal-Bendirdjian, “Staurosporine induces apoptosis through both caspase-dependent and caspase-independent mechanisms,” *Oncogene*, vol. 20, no. 26, pp. 3354–3362, 2001.
[37] A. M. Lawrie, M. E. Noble, P. Tunnah, N. R. Brown, L. N. Johnson, and J. A. Endicott, “Protein kinase inhibition by staurosporine revealed in details of the molecular interaction with CDK2,” *Nature structural biology*, vol. 4, no. 10, pp. 796–801, 1997.
[38] T.-L. Yue *et al.*, “Staurosporine-induced apoptosis in cardiomyocytes: a potential role of caspase-3,” *Journal of molecular and cellular cardiology*, vol. 30, no. 3, pp. 495–507, 1998.
[39] D. Wlodkowic, J. Skommer, and Z. Darzynkiewicz, “Flow Cytometry-Based Apoptosis Detection,” in *Apoptosis*, vol. 559, P. Erhardt and A. Toth, Eds., in Methods in Molecular Biology, vol. 559. , Totowa, NJ: Humana Press, 2009, pp. 19–32. doi: 10.1007/978-1-60327-017-5_2.
[40] S. Toné *et al.*, “Three distinct stages of apoptotic nuclear condensation revealed by time-lapse imaging, biochemical and electron microscopy analysis of cell-free apoptosis,” *Experimental cell research*, vol. 313, no. 16, pp. 3635–3644, 2007.
[41] M. G. Ormerod, X. Sun, R. T. Snowden, R. Davies, H. Fearnhead, and G. M. Cohen, “Increased membrane permeability of apoptotic thymocytes: A flow cytometric study,” *Cytometry*, vol. 14, no. 6, pp. 595–602, Aug. 1993, doi: 10.1002/cyto.990140603.
[42] T. D. O’Connell *et al.*, “The α 1A/C-and α 1B-adrenergic receptors are required for physiological cardiac hypertrophy in the double-knockout mouse,” *The Journal of clinical investigation*, vol. 111, no. 11, pp. 1783–1791, 2003.
[43] K. A. Ryall and J. J. Saucerman, “Automated imaging reveals a concentration dependent delay in reversibility of cardiac myocyte hypertrophy,” *Journal of Molecular and Cellular Cardiology*, vol. 53, no. 2, pp. 282–290, 2012.
[44] T. D. O’Connell, B. C. Jensen, A. J. Baker, and P. C. Simpson, “Cardiac alpha1-adrenergic receptors: novel aspects of expression, signaling mechanisms, physiologic function, and clinical importance,” *Pharmacological reviews*, vol. 66, no. 1, pp. 308–333, 2014.

[45] T. Schneider-Poetsch *et al.*, “Inhibition of eukaryotic translation elongation by cycloheximide and lactimidomycin,” *Nature chemical biology*, vol. 6, no. 3, pp. 209–217, 2010.
[46] G. Bass *et al.*, “Automated image analysis identifies signaling pathways regulating distinct signatures of cardiac myocyte hypertrophy.,” *Journal of molecular and cellular cardiology*, vol. 52, no. 5, pp. 923–930, May 2012, doi: 10.1016/j.yjmcc.2011.11.009.
[47] Z. Liu, S. Yue, X. Chen, T. Kubin, and T. Braun, “Regulation of Cardiomyocyte Polyploidy and Multinucleation by CyclinG1,” *Circulation Research*, vol. 106, no. 9, pp. 1498–1506, May 2010, doi: 10.1161/CIRCRESAHA.109.211888.
[48] L. A. Woo *et al.*, “High-content phenotypic assay for proliferation of human iPSC-derived cardiomyocytes identifies L-type calcium channels as targets,” *J Mol Cell Cardiol*, vol. 127, pp. 204–214, Feb. 2019, doi: 10.1016/j.yjmcc.2018.12.015.
[49] R. Imai *et al.*, “Density imaging of heterochromatin in live cells using orientation-independent-DIC microscopy,” *MBoC*, vol. 28, no. 23, pp. 3349–3359, Nov. 2017, doi: 10.1091/mbc.e17-06-0359.
[50] S. T. Homa, S. D. Webster, and R. K. Russell, “Phospholipid turnover and ultrastructural correlates during spontaneous germinal vesicle breakdown of the bovine oocyte: effects of a cyclic AMP phosphodiesterase inhibitor,” *Developmental biology*, vol. 146, no. 2, pp. 461–472, 1991.
[51] D. A. Rew and G. D. Wilson, “Cell production rates in human tissues and tumours and their significance. Part II: clinical data,” *European Journal of Surgical Oncology (EJSO)*, vol. 26, no. 4, pp. 405–417, 2000.
[52] J. Yang, R. Polanowska-Grabowska, J. Smith, C. Shields, and J. Saucerman, “PKA catalytic subunit compartmentation regulates contractile and hypertrophic responses to β-adrenergic signaling.,” *Journal of molecular and cellular cardiology*, vol. 66C, pp. 83–93, Nov. 2013, doi: 10.1016/j.yjmcc.2013.11.001.
[53] M. Zaugg, W. Xu, E. Lucchinetti, S. A. Shafiq, N. Z. Jamali, and M. A. Q. Siddiqui, “β-Adrenergic Receptor Subtypes Differentially Affect Apoptosis in Adult Rat Ventricular Myocytes,” *Circulation*, vol. 102, no. 3, pp. 344–350, Jul. 2000, doi: 10.1161/01.CIR.102.3.344.
[54] C. Communal, K. Singh, D. R. Pimentel, and W. S. Colucci, “Norepinephrine Stimulates Apoptosis in Adult Rat Ventricular Myocytes by Activation of the β-Adrenergic Pathway,” *Circulation*, vol. 98, no. 13, pp. 1329–1334, Sep. 1998, doi: 10.1161/01.CIR.98.13.1329.
[55] Y. Zou *et al.*, “Isoproterenol activates extracellular signal-regulated protein kinases in cardiomyocytes through calcineurin,” *Circulation*, vol. 104, no. 1, pp. 102–108, Jul. 2001, doi: 10.1161/hc2601.090987.
[56] H. Zhu, S. McElwee-Witmer, M. Perrone, K. L. Clark, and A. Zilberstein, “Phenylephrine protects neonatal rat cardiomyocytes from hypoxia and serum deprivation-induced apoptosis,” *Cell Death Differ*, vol. 7, no. 9, Art. no. 9, Sep. 2000, doi: 10.1038/sj.cdd.4400721.
[57] X.-Z. Zhuo *et al.*, “Isoproterenol instigates cardiomyocyte apoptosis and heart failure via AMPK inactivation-mediated endoplasmic reticulum stress,” *Apoptosis*, vol. 18, no. 7, pp. 800–810, Jul. 2013, doi: 10.1007/s10495-013-0843-5.
[58] B. Ding *et al.*, “Functional Role of Phosphodiesterase 3 in Cardiomyocyte Apoptosis,” *Circulation*, vol. 111, no. 19, pp. 2469–2476, May 2005, doi: 10.1161/01.CIR.0000165128.39715.87.
[59] F. Bonavita *et al.*, “H9c2 cardiac myoblasts undergo apoptosis in a model of ischemia consisting of serum deprivation and hypoxia: inhibition by PMA,” *FEBS letters*, vol. 536, no. 1–3, pp. 85–91, 2003.
[60] S. Bialik *et al.*, “The Mitochondrial Apoptotic Pathway Is Activated by Serum and Glucose Deprivation in Cardiac Myocytes,” *Circulation Research*, vol. 85, no. 5, pp. 403–414, Sep. 1999, doi: 10.1161/01.RES.85.5.403.

[61] M. Boutros, F. Heigwer, and C. Laufer, “Microscopy-Based High-Content Screening,” *Cell*, vol. 163, no. 6, pp. 1314–1325, Feb. 2016, doi: 10.1016/j.cell.2015.11.007.
[62] G. Sugihara *et al.*, “Detecting Causality in Complex Ecosystems,” *Science*, vol. 338, no. 6106, pp. 496–500, Oct. 2012, doi: 10.1126/science.1227079.
[63] M. Vilela and G. Danuser, “What’s wrong with correlative experiments?,” *Nat Cell Biol*, vol. 13, no. 9, pp. 1011–1011, Sep. 2011, doi: 10.1038/ncb2325.
[64] A. L. Koenig *et al.*, “Single-cell transcriptomics reveals cell-type-specific diversification in human heart failure,” *Nat Cardiovasc Res*, vol. 1, no. 3, pp. 263–280, Mar. 2022, doi: 10.1038/s44161-022-00028-6.
[65] N. R. Tucker *et al.*, “Transcriptional and Cellular Diversity of the Human Heart,” *Circulation*, vol. 142, no. 5, pp. 466–482, Aug. 2020, doi: 10.1161/CIRCULATIONAHA.119.045401.
[66] M. van Bilsen and K. R. Chien, “Growth and hypertrophy of the heart: towards an understanding of cardiac specific and inducible gene expression,” *Cardiovascular research*, vol. 27, no. 7, pp. 1140–1149, 1993.
[67] C.-Y. Tsai *et al.*, “E2/ER β inhibit ISO-induced cardiac cellular hypertrophy by suppressing Ca2+-calcineurin signaling,” *PLoS One*, vol. 12, no. 9, p. e0184153, 2017.
[68] A. M. Heijink *et al.*, “Modeling of cisplatin-induced signaling dynamics in triple-negative breast cancer cells reveals mediators of sensitivity,” *Cell reports*, vol. 28, no. 9, pp. 2345–2357, 2019.
[69] A. L. Paek, J. C. Liu, A. Loewer, W. C. Forrester, and G. Lahav, “Cell-to-cell variation in p53 dynamics leads to fractional killing,” *Cell*, vol. 165, no. 3, pp. 631–642, 2016.
[70] M. Fallahi□Sichani *et al.*, “Adaptive resistance of melanoma cells to RAF inhibition via reversible induction of a slowly dividing de□differentiated state,” *Molecular Systems Biology*, vol. 13, no. 1, p. 905, Jan. 2017, doi: 10.15252/msb.20166796.
[71] K. M. Kovary, B. Taylor, M. L. Zhao, and M. N. Teruel, “Expression variation and covariation impair analog and enable binary signaling control,” *Molecular Systems Biology*, vol. 14, no. 5, p. e7997, May 2018, doi: 10.15252/msb.20177997.
[72] A. Hilfinger and J. Paulsson, “Separating intrinsic from extrinsic fluctuations in dynamic biological systems,” *Proc. Natl. Acad. Sci. U.S.A.*, vol. 108, no. 29, pp. 12167–12172, Jul. 2011, doi: 10.1073/pnas.1018832108.
[73] P. S. Swain, M. B. Elowitz, and E. D. Siggia, “Intrinsic and extrinsic contributions to stochasticity in gene expression,” *Proc. Natl. Acad. Sci. U.S.A.*, vol. 99, no. 20, pp. 12795–12800, Oct. 2002, doi: 10.1073/pnas.162041399.
[74] C.-F. Liu and W. H. W. Tang, “Epigenetics in Cardiac Hypertrophy and Heart Failure,” *JACC: Basic to Translational Science*, vol. 4, no. 8, pp. 976–993, Dec. 2019, doi: 10.1016/j.jacbts.2019.05.011.
[75] O. Symmons and A. Raj, “What’s luck got to do with it: single cells, multiple fates, and biological nondeterminism,” *Molecular cell*, vol. 62, no. 5, pp. 788–802, 2016.
[76] A. Piek, R. A. De Boer, and H. H. W. Silljé, “The fibrosis-cell death axis in heart failure,” *Heart Fail Rev*, vol. 21, no. 2, pp. 199–211, Mar. 2016, doi: 10.1007/s10741-016-9536-9.
[77] S. M. Gross, M. A. Dane, E. Bucher, and L. M. Heiser, “Individual cells can resolve variations in stimulus intensity along the IGF-PI3K-AKT signaling axis,” *Cell systems*, vol. 9, no. 6, pp. 580–588, 2019.
[78] H. Honkoop, P. D. Nguyen, V. E. M. van der Velden, K. F. Sonnen, and J. Bakkers, “Live imaging of adult zebrafish cardiomyocyte proliferation ex vivo,” *Development*, vol. 148, no. 18, p. dev199740, Sep. 2021, doi: 10.1242/dev.199740.
[79] S. Sawamiphak, Z. Kontarakis, A. Filosa, S. Reischauer, and D. Y. R. Stainier, “Transient cardiomyocyte fusion regulates cardiac development in zebrafish,” *Nat Commun*, vol. 8, no. 1, p. 1525, Nov. 2017, doi: 10.1038/s41467-017-01555-8.

[80] M. Zhang, K. O. Lui, and B. Zhou, “Application of New Lineage Tracing Techniques in Cardiovascular Development and Physiology,” *Circulation Research*, vol. 134, no. 4, pp. 445–458, Feb. 2024, doi: 10.1161/CIRCRESAHA.123.323179.

[81] L. Wang, J. S. Brugge, and K. A. Janes, “Intersection of FOXO- and RUNX1-mediated gene expression programs in single breast epithelial cells during morphogenesis and tumor progression,” *Proc. Natl. Acad. Sci. U.S.A.*, vol. 108, no. 40, Oct. 2011, doi: 10.1073/pnas.1103423108.

[82] S. S. Bajikar, C.-C. Wang, M. A. Borten, E. J. Pereira, K. A. Atkins, and K. A. Janes, “Tumor-suppressor inactivation of GDF11 occurs by precursor sequestration in triple-negative breast cancer,” *Developmental cell*, vol. 43, no. 4, pp. 418–435, 2017.

[83] S. Berg *et al.*, “Ilastik: interactive machine learning for (bio) image analysis,” *Nature methods*, vol. 16, no. 12, pp. 1226–1232, 2019.

[84] H. Wickham *et al.*, “Welcome to the Tidyverse,” *JOSS*, vol. 4, no. 43, p. 1686, Nov. 2019, doi: 10.21105/joss.01686.

[85] T. Hothorn, F. Bretz, and P. Westfall, “Simultaneous inference in general parametric models,” *Biom J*, vol. 50, no. 3, pp. 346–363, Jun. 2008, doi: 10.1002/bimj.200810425.

[86] J. Pinheiro, “nlme: Linear and nonlinear mixed effects models,” *R package version*, vol. 3, p. 1, 2011.

[87] F. Kemp, “Modern applied statistics with S.” Oxford University Press, 2003. Accessed: Oct. 14, 2024. [Online]. Available: https://academic.oup.com/jrsssd/article-abstract/52/4/704/7123905

[88] J. Hendrickx and M. J. Hendrickx, “Package ‘perturb,’” 2019, Accessed: Oct. 14, 2024. [Online]. Available: https://citeseerx.ist.psu.edu/document?repid=rep1&type=pdf&doi=8e092b5cf100818c3caaee8c9dec2f0d8014a9f2

[89] T. Pohlert, “PMCMRplus: Calculate pairwise multiple comparisons of mean rank sums extended. R package version 1.9. 6,” *PMCMRplus: Calculate Pairwise Multiple Comparisons of Mean Rank Sums Extended*, 2018.

[90] A. Liaw, “Classification and regression by randomForest,” *R news*, 2002.

[91] M. Hlavac, “Stargazer: Well-formatted regression and summary statistics tables,” *R package version*, vol. 5, no. 2, p. 2, 2018.

[92] E. Kwan and M. Friendly, “tableplot: Represents tables as semi-graphic displays,” *R package version 03-5*, 2012.

[93] W. N. Venables and B. D. Ripley, *Modern Applied Statistics with S*, 4th ed. in Statistics and Computing. New York: Springer-Verlag, 2002. doi: 10.1007/978-0-387-21706-2.

Supplemental Figures

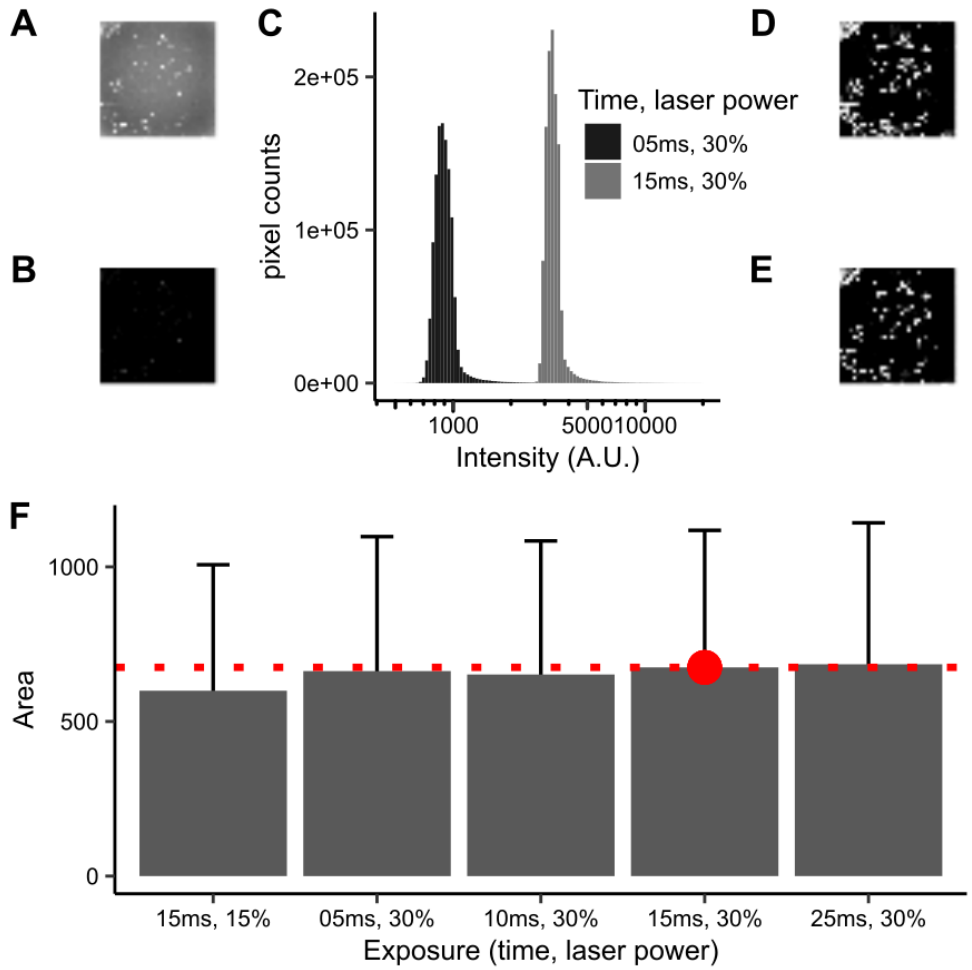

Supplemental Figure 1. Segmentation on eGFP fluorescence probability maps is robust to 5-fold variation in signal-to-noise ratio.
The same field of view of cells was taken with either 15 ms (A) or 5 ms (B) of exposure with 30% laser power.
(C) Image intensity histogram of the two images. The same Ilastik random forest model was used to generate GFP fluorescence probability maps of the images taken with either 15 ms (D) or 5ms (E) of exposure.
(F) Single-cell area distributions were compared with varying signal-to-noise ratios generated by varying exposure duration or laser power.

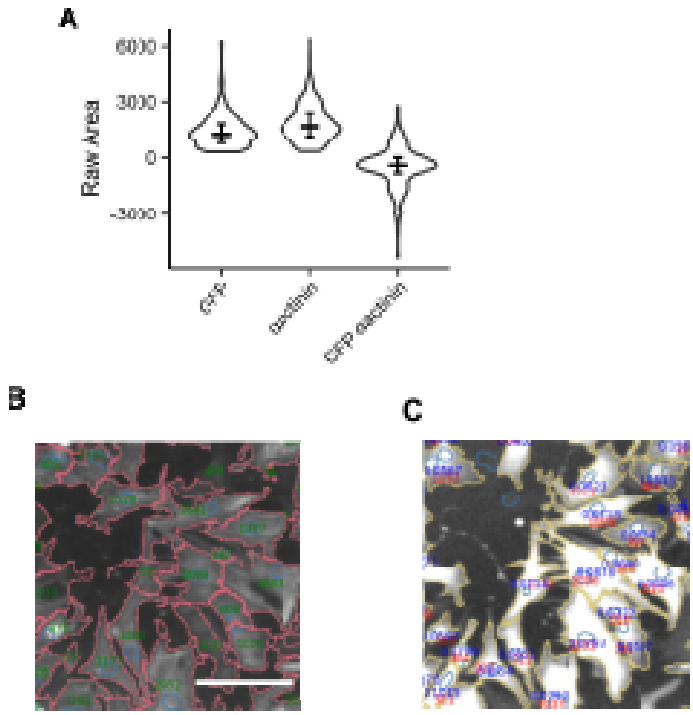

Supplemental Figure 2. GFP watershed algorithm provides better fidelity to actual cell areas

(**A**) Areas of GFP and □-actinin double-positive cells segmented in GFP or □-actinin channels, and the difference between the two. Solid lines indicate population median, error bars indicate interquartile range.

Segmentation borders of □-actinin (**B**, red), or GFP (**C**, yellow) fluorescence. Green numbers in (**B**) or red numbers in (**C**) indicate cell areas. Blue numbers in (**C**) indicate GFP fluorescence intensity.

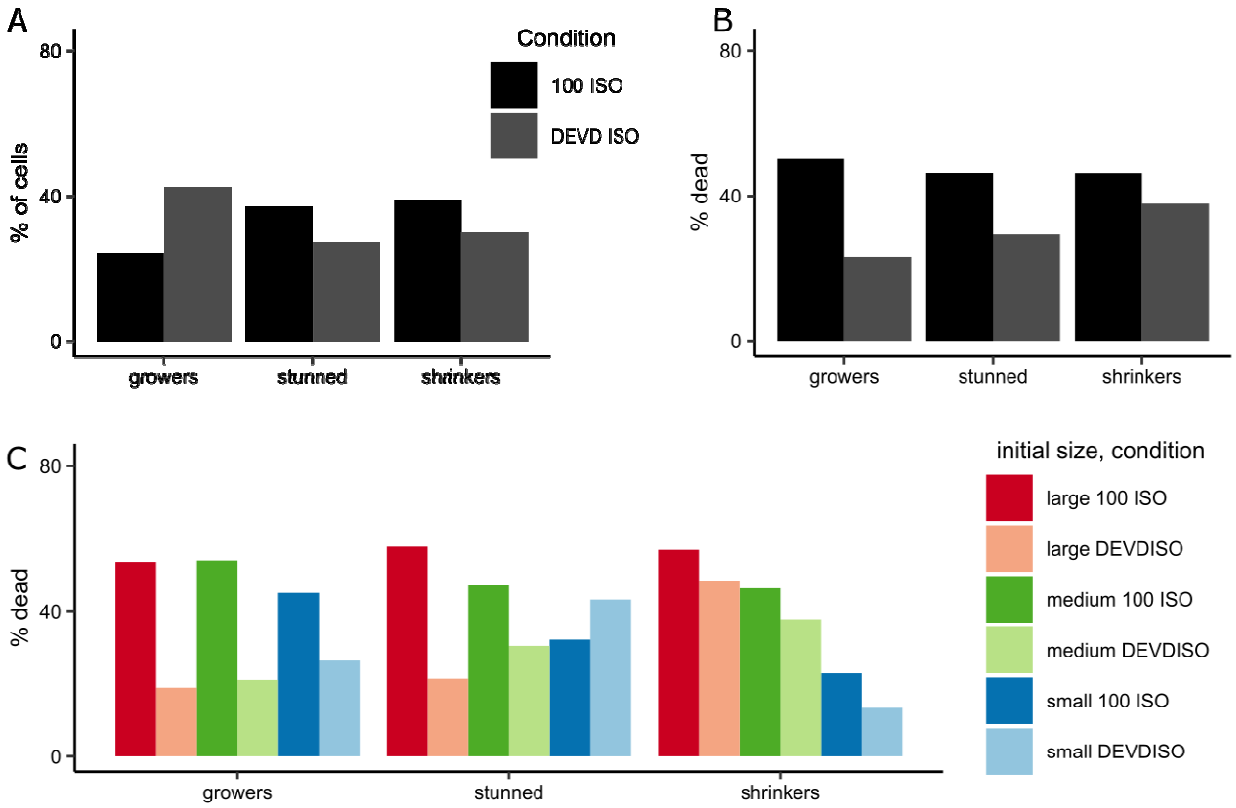

Supplemental Figure 3. Caspase-3 inhibitor Z-DEVD-FMK inhibits ISO-induced apoptosis and increases grower cell subpopulation.
(**A**) Addition of 20 µM Z-DEVD-FMK increases the proportion of grower cells while decreasing the proportion of shrinker cells.
(**B**) Addition of Z-DEVD-FMK decreases the death rates of each growth subpopulation.
(**C**) Addition of Z-DEVD-FMK decreases the death rates of each growth subpopulation except for the initially small, stunned growth subpopulation.

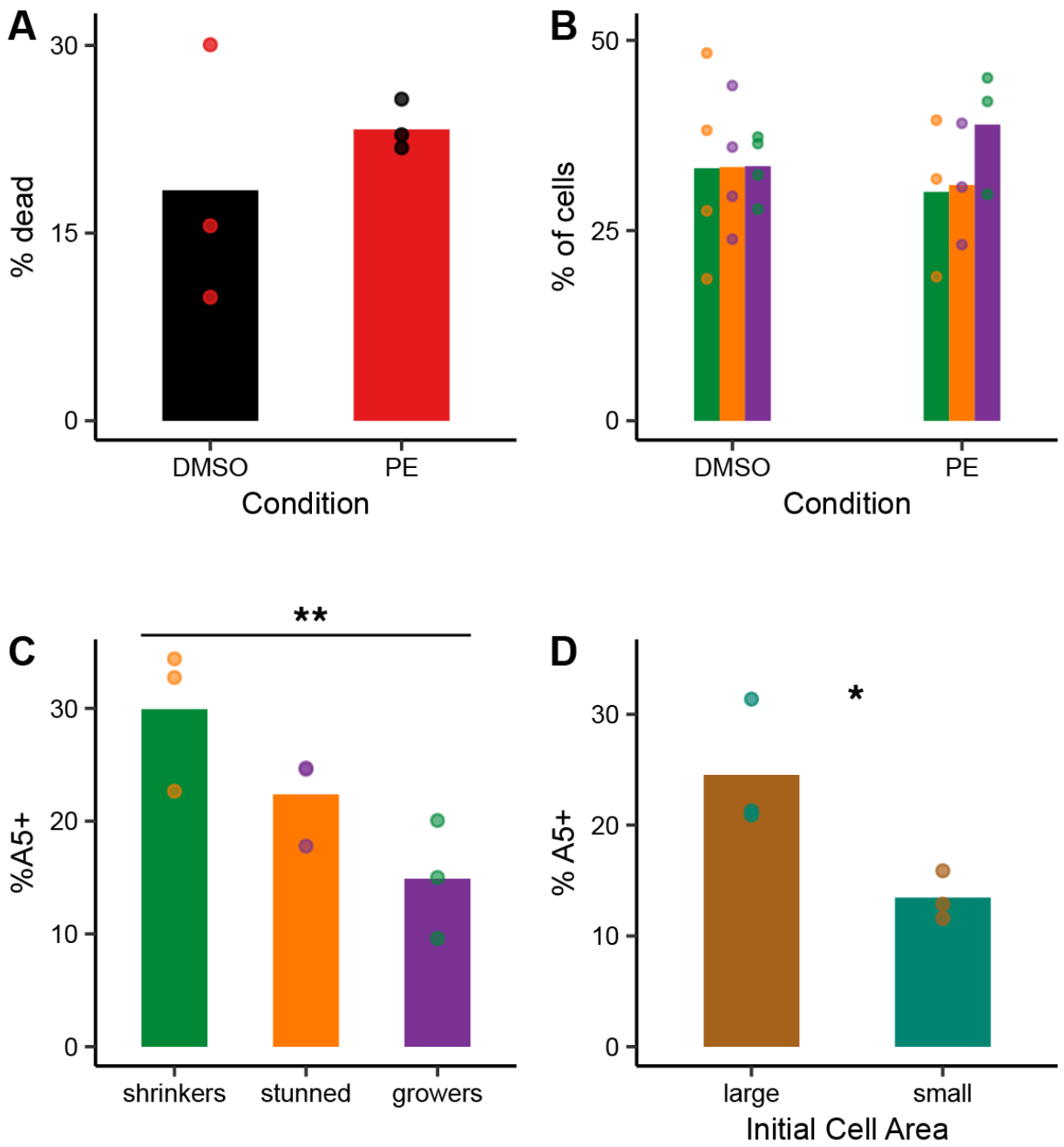

Supplemental Figure 4. Phenylephrine increases apoptosis-resistant grower cell subpopulation.
(**A**) Addition of 50 µM PE does not affect rate of cell death. p = 0.427, one-sided Welch's paired *t*-test, 1-3 wells for each condition from n = 3 independent cell isolations.
(**B**) Addition of PE increases the proportion of grower subpopulation. p = 0.121, mixed effects ANOVA with post-hoc Dunnett's test and Bonferroni correction. 1-3 wells for each subpopulation per each condition from n = 3-4 independent cell isolations.
(**C**) While the overall mixed-effects ANOVA was not statistically significant (p=0.063) the greater-powered Tukey HSD test showed that the grower subpopulation was more resistant to apoptosis than the shrinker subpopulation (**p < 0.01, 1-3 wells for each subpopulation from n = 3 independent cell isolations).

(**D**) PE-treated cells in the largest quartile of initial cell areas were more likely to die than cells in the smallest quartile. * p = 0.019, one-sided Welch's paired *t*-test, 1-3 wells for each condition from n = 3 independent cell isolations.

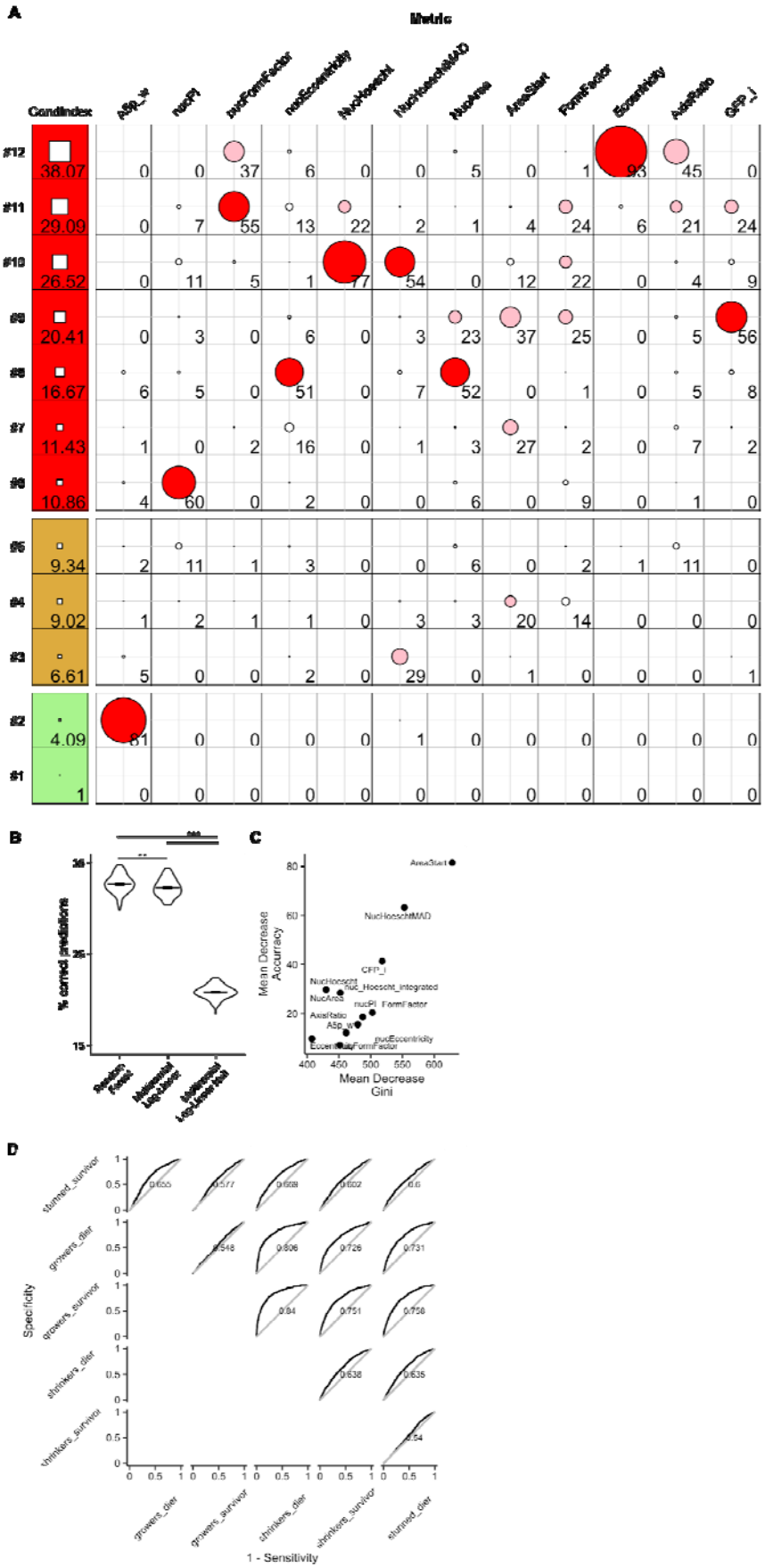
A
Metric
Condindex
A5p_w
nucPI
nucFormFactor
nucEccentricity
NucHoeschtMAD
NucArea
AreaStart
FormFactor
Eccentricity
AxisRatio
GFP_i
#12 38.07 0 0 37 6 0 0 5 0 1 93 45 0
#11 29.09 0 7 55 13 22 2 1 4 24 6 21 24
#10 26.52 0 11 5 1 77 54 0 12 22 0 4 9
#9 20.41 0 3 0 6 0 3 23 37 25 0 5 56
#8 16.67 6 5 0 51 0 7 52 0 1 0 5 8
#7 11.43 1 0 2 16 0 1 3 27 2 0 7 2
#6 10.86 4 60 0 2 0 0 6 0 9 0 1 0
#5 9.34 2 11 1 3 0 0 6 0 2 1 11 0
#4 9.02 1 2 1 1 0 3 3 20 14 0 0 0
#3 6.61 5 0 0 2 0 29 0 1 0 0 0 1
#2 4.09 81 0 0 0 0 1 0 0 0 0 0 0
#1 1 0 0 0 0 0 0 0 0 0 0 0
B
% correct predictions
C
Mean Decrease Accuracy
Mean Decrease Gini
AreaStart
NucHoeschtMAD
CFP_i
NucHoescht
nuc_Hoescht_integrated
NucArea
nucPI
FormFactor
AxisRatio
A5p_w
nucEccentricity
Eccentricity
FormFactor
D
Specificity
1 - Sensitivity
stunned_survivor
growers_dier
growers_survivor
shrinkers_dier
shrinkers_survivor
0.655
0.577
0.669
0.602
0.6
0.548
0.806
0.726
0.731
0.84
0.751
0.758
0.638
0.635
0.54

973 **Supplemental Figure 5. Colinearity of predictor variables and comparison of**
974 **model performances.**
975 (**A**) Tableplot of Condition indices and coefficient variance proportions [90]. Briefly, condition
976 indices represent scaled eigenvalues of the correlation matrix among the predictors variables.
977 The condition index box is green for indexes less than 5, yellow if less than 10, and red if greater
978 than 10. Each row represents an eigenvector with the "metric" columns corresponding to each
979 predictor variable's proportion of variance scaled to 100.
980 (**B**) 5-fold cross-validation accuracy. Error bars represent mean ± SEM. **p = 0.002, ***p <
981 $2*10^{-22}$, repeated-measured ANOVA followed by paired T-test with Benjamini-Hochberg
982 correction for multiple comparisons, n=100 random partitions.
983 (**C**) Random forest predictor variable importance measures.
984 (**D**) Multiclass and pairwise AUC curves.
985
986

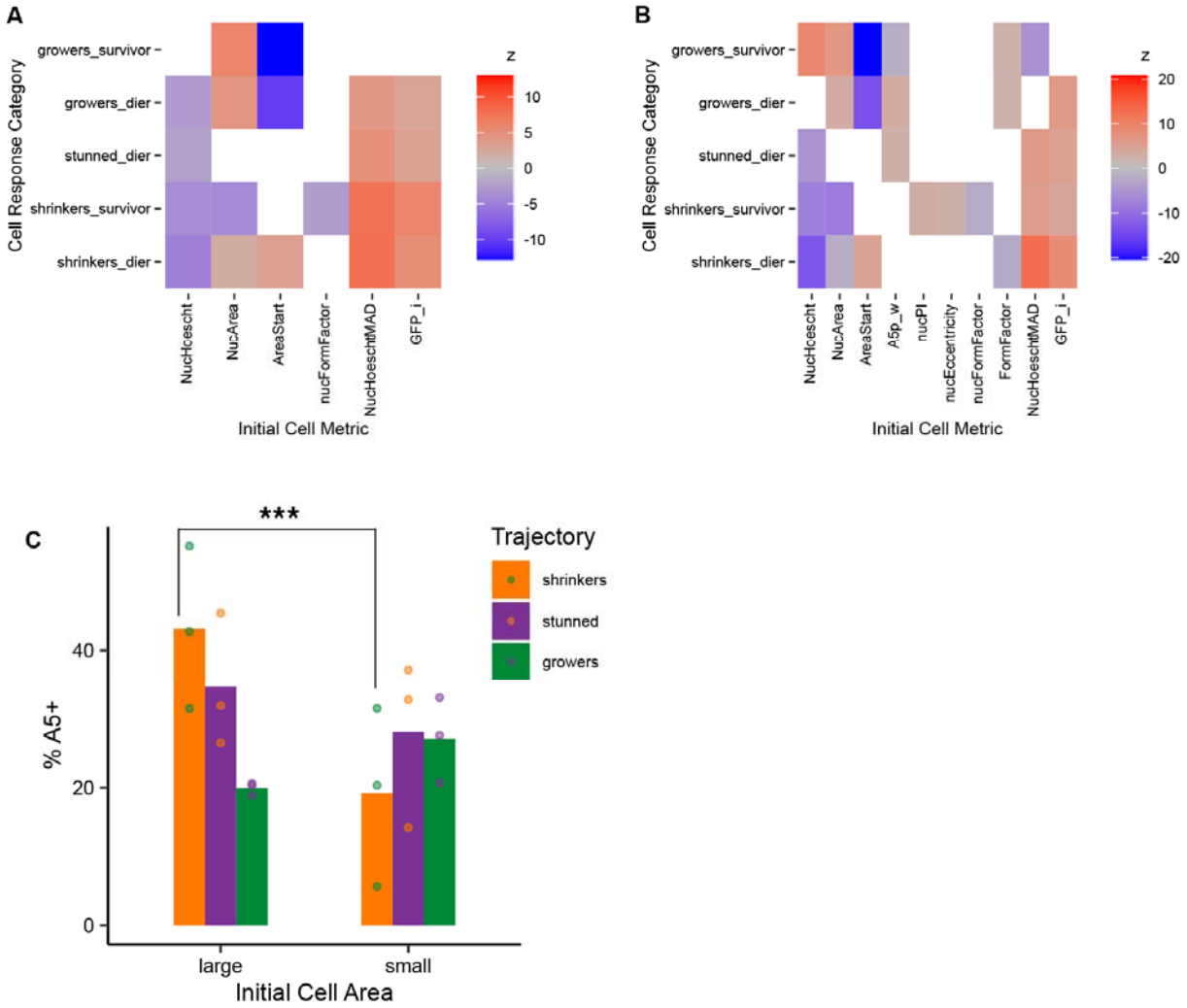

987
988 **Supplemental Figure 6. Multinomial log-linear model coefficients for PE and 56.2**
989 **µM ISO.**
990 (**A**) Model for 50 µM PE.

(**B**) Model for 56.2 μM ISO.
(**C**) Apoptosis rate by initial cell area and growth trajectory. *** p = 0.00044, one-sided Welch's paired *t*-test, 1-3 wells for each condition from n = 3 independent cell isolations.

Supplemental Tables

Supplemental Table 1. **Multinomial log-linear regressions predicting hypertrophy-apoptosis phenotype likelihood relative to the stunned survivor phenotype.** Values are represented as the regression coefficients and standard errors in parentheses. Akaike Information Criterion = 30818.4

	Dependent variable:				
	growers_dier	growers_survivor	shrinkers_dier	shrinkers_survivor	stunned_dier
	(1)	(2)	(3)	(4)	(5)
A5p_w	-0.247	-0.601***	-0.089	-0.108	0.058
	(0.200)	(0.173)	(0.178)	(0.166)	(0.194)
nucPI	0.615	0.326	2.405***	1.310**	0.313
	(0.648)	(0.572)	(0.552)	(0.538)	(0.636)
nucFormFactor	0.566	-0.159	0.433	-0.679*	0.553
	(0.452)	(0.372)	(0.397)	(0.365)	(0.439)

nucEccentricity	-0.160	-0.201	0.471*	0.369	0.552*
	(0.313)	(0.265)	(0.282)	(0.265)	(0.311)
NucHoescht	-0.162	2.559***	-11.594***	-7.476***	-5.250***
	(0.889)	(0.762)	(0.853)	(0.789)	(0.896)
NucHoeschtMAD	1.540*	-4.929***	14.391***	8.033***	8.553***
	(0.786)	(0.688)	(0.717)	(0.666)	(0.763)
NucArea	2.486***	2.450***	-1.229*	-3.251***	0.570
	(0.725)	(0.588)	(0.632)	(0.586)	(0.700)
AreaStart	-9.710***	-7.923***	4.959***	2.037***	0.750
	(0.685)	(0.532)	(0.461)	(0.452)	(0.531)
FormFactor	0.802***	0.685***	-0.017	0.151	0.311
	(0.309)	(0.265)	(0.275)	(0.262)	(0.301)
Eccentricity	0.018	0.277	0.220	-0.099	-0.104

	(0.404)	(0.345)	(0.364)	(0.336)	(0.392)
AxisRatio	-1.123	-0.701	-0.443	0.357	-0.034
	(0.792)	(0.634)	(0.629)	(0.572)	(0.694)
GFP_i	4.564***	-0.182	5.490***	2.564***	4.590***
	(0.718)	(0.688)	(0.640)	(0.633)	(0.697)
Constant	-1.182	1.363*	-2.813***	1.057	-3.031***
	(0.903)	(0.769)	(0.802)	(0.745)	(0.882)

Note: *p<0.1; **p<0.05; ***p<0.01

Supplemental Movies

Supplemental Movie 1. Live single cell tracking of DMSO-treated neonatal rat cardiomyocytes across 48 hours. Frames were sampled once per hour (0-48 hrs, 49 frames total). Left panel shows merged raw images of Hoechst (blue) and GFP (green) stains. Middle panel shows automated CellProfiler segmentation and nuclei tracking of cells. Right panel shows merged Annexin V (yellow) and PI (magenta) stains. Scale = 100μm.

Supplemental Movie 2. Live single cell tracking of staurosporine (STS)-treated neonatal rat cardiomyocytes across 48 hours. Cardiomyocytes treated with μM STS show increased rates of apoptosis and cell death.

Supplemental Movie 3. Live single cell tracking of phenylephrine (PE)-treated neonatal rat cardiomyocytes across 48 hours. Cardiomyocytes treated with 50 μM PE induce a hypertrophic response shown by an increase in cell area and GFP expression

Supplemental Movie 4. Live single cell tracking of 10 μM isoproterenol (ISO)-treated cells across 48 hours. Cells treated with 10μM ISO show mixed responses of apoptosis and hypertrophy.

Supplemental Movie 5. Live single cell tracking of 100 μM ISO-treated cells across 48 hours. Cardiomyocytes treated with 100 μM ISO show both hypertrophy and apoptotic responses but shift towards apoptosis at the end.

1021